

Mitigation of Hot Cracking Susceptibility in Laser Welding of Transformation Induced Plasticity Steels by Beam Shaping

**An Experimental Approach** 

Author: Junhong Li Date: 20 December, 2024



# Mitigation of Hot Cracking Susceptibility in Laser Welding of Transformation Induced Plasticity Steels by Beam Shaping

## **An Experimental Approach**

by

### Junhong Li

In partial fulfilment of the requirements for the degree of:

#### **Master of Science**

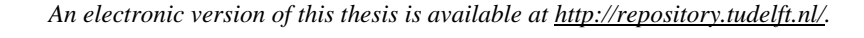
in Materials Science and Engineering

at the Delft University of Technology, to be defended publicly on [Friday December 20, 2024, at 11:30 AM.]

Supervisor: Dr. M. J. M. Hermans

Thesis committee: Dr. G. Filonenko, TU Delft

Dr. A. Ebrahimi. TNO





### **Abstract**

Hot cracking is a significant imperfection in laser welding of thin transformation induced plasticity (TRIP) steel sheets. This study aims to evaluate strategies to mitigate the hot cracking susceptibility through beam shaping, by performing free edge welding tests. TRIP steel sheets were welded with a laser beam with a constant laser power for various spot sizes and incident angles at different distances from the free edge. A high-speed camera and a welding camera are applied to film the behaviour of the plasma plume and the development of the molten fluid flow. Pre-attached thermocouples are utilized for insitu transient temperature measurements. The weld pool dimensions and microstructures of the fusion zones are characterized by optical microscopy and semi-quantitative elemental analysis is conducted by scanning electron microscopy and energy dispersive spectroscopy (SEM-EDS). Experiments showed that, as the heat input increases, the vaporization of material induces a recoil pressure and leads to keyhole formation, and the direction of maximum thermal gradient and the cooling rate determines the microstructure. At a fixed beam spot size and incident angle, an increased travel speed decreases the heat input, and results in a smaller bead width with less solidification shrinkage and thermal contraction. In the case of varying spot sizes with a fixed incident angle and travel speed, a small spot size of 0.2 mm refers to a high energy density, the concentrated beam creates an open keyhole that leads to energy loss, and the absorption rate of thermal energy is low. Such a condition generates a narrow bead width, which results in less shrinkage that mitigates the hot cracking susceptibility significantly. When the spot size increases, a wider bead is created that enhances the contraction and therefore higher tensile stresses, which causes the metal to be more prone to cracking. When the diameter of the spot increases to 1.2 mm, the thermal energy is so dispersed that the heat is not sufficient to evaporate significant amounts of metal and the operation mode switches from a keyhole mode to a conduction mode, which only partially penetrates the steel sheet. In the case of varying the incident angle with a fixed spot width and fixed travel speed, the inclined beam projects a prolonged elliptical impingement area and shifts the location of highest density according to the incident angle. A leading beam configuration, i.e. a small incident angle, acts as post-heating source of the molten liquid. For large incident angles of a trailing configuration, the beam impinges on the front wall of the keyhole and acts as a pre-heating source. A prolonged elliptical heated area increases the time for the back feeding liquid to heal the gaps between the columnar grains growing into the fusion zone and suppresses the hot cracking susceptibility. If the incident angle becomes too small (45°), the consequence is similar to a too dispersed spot size, i.e. partial penetration of the sheet. A trailing configurated beam can reflect on the front keyhole wall and enhances absorption, but it generates turbulent flow. When the angle comes too large (135°), the process is not entirely stable. In conclusion, for producing defect-free welds in industrial applications, it is recommended to utilize a small spot size that corresponds to less solidification shrinkage. Furthermore, a leading configuration is preferred, but the incident angle should not be too low, in order to achieve full penetration.

# Keywords

joining; welding; laser welding; hot cracking; material; metal; steel; high strength steel; susceptibility; hot cracking susceptibility; weldability.

## Acknowledgement

I would hereby like to show all my gratefulness to everyone I worked with, and everyone gave me help along my journey to become a qualified Master of Materials Science and Engineering.

First of all, I would like to sincerely thank to the faculty of Mechanical Engineering, Delft University of Technology, for giving me the opportunity to study and achieve my goal. Especially for my supervisor dr. Marcel Hermans and dr. Amin Ebrahimi, who always correct my reports detailly and paid much patience for guiding me.

During my experiment work, I would like to express my gratefulness to Jurriaan van Slingerland, the technician of the laser lab. Along my research experience, I used to have a difficult time, when the laser system was malfunctioned. I am quite moved by the hard work that Jurriaan spent for repairing the system and contacting the manufacturer.

I would like to thank Arjun Sood as well. As my senior, he gave me a lot of useful advice and inspired me in achieving a satisfied reference setup in preliminary experiments. The Cavitar® welding camera he provided also aided me for observing the melt pool behaviour during welding and ensured me to do more detailed analyses.

In terms of my daily lives, I am grateful for parents and my relatives, who provided me with financial support along the past years abroad, and always stand by me. Especially my great-aunt, who mailed me winter clothes and paid me lots of concerns.

Last but not least, I would sincerely express my thanks to China Food Newspaper, which is the news agency I worked at as a part-time journalist, and all my production team members of BanG Dream! Spring Festival Gala. The precious cooperation experience always reminds me to shoulder my social responsibilities and encourages me to be responsible for my academic research.

Junhong Li Delft. December 2024

## **Contents**

Al	bstract	5
A	cknowledgement	7
No	omenclature	11
1	Introduction	13
2	Experimental	21
3	Results	26
	3.1 Impact of Welding Speed	26
	3.2 Impact of Beam Spot Diameter	28
	3.3 Impact of Incident Angle in Longitudinal Direction	32
	3.4 Fluid Flow Behaviour	38
	3.4.1 Keyhole Mode	38
	3.4.2Conduction Mode	39
	3.5 Transient Temperature	40
	3.6 Hot Cracking Susceptibility	42
	3.7 Microstructure	43
4	Disscussion	48
5	Conclusion	53
Bi	ibliography	54

# Nomenclature

Symbol	Definition	Unit
$\boldsymbol{A}$	absorption rate	/
d	beam spot diameter	mm
G	temperature gradient	
I	intensity of laser	$W/m^2$
$I_0$	peak intensity of laser	$W/m^2$
k	extinction index	/
n	refractive index	/
P	laser power	kW
$Q_0$	maximum heat flux	$Wm^{-3}$
$Q_{v}$	heat flux at any place perpendicular to the z-axis	$Wm^{-3}$
Ŕ	solidification rate	
r	distance from the central axis	m
$r_c$	flux distribution parameter	m
$r_e$	larger radii of the cone of the Gaussian beam	m
$r_i$	smaller radii of the cone of the Gaussian beam	m
V	travel speed	mm/s
$z_e$	upper coordinate of the cone of the Gaussian beam	m
$Z_i$	lower coordinate of the cone of the Gaussian beam	m
ά	incident angle	0
γ	surface tension coefficient	
$\eta$	process efficiency	/
λ	wavelength of laser	μm
σ	the width where the intensity $I$ equals to $\frac{1}{e^2}$ times of the peak intensity $I_0$	•

Abbreviation	Definition
AHSS	Advanced High Strength
BTR	Brittle Temperature Range
EDS	Energy Dispersive Spectroscopy
HAZ	Heat Affected Zone
HSS	High Strength Steel
NDT	Non-Destructive Test
Nd:YAG	Neodymium-Doped Yttrium Aluminum Garnet
SEM	Scanning Electron Microscope
TRIP	Transformation Induced Plasticity

### 1 Introduction

High strength steels (HSS) and advanced high strength steels (AHSS) are extensively utilized in various sectors including architecture, automotive, and aerospace structures (Ban & Shi, 2018) (Xinhua News, 2024), attribute to the high strength and ductility (Ban & Shi, 2018). However, hot cracking is a significant imperfection in laser welding of thin high strength steel sheets (Farid & Molian, 2000) (Kannengießer & Böllinghaus, 2014). Hot cracks are often challenging to detect through non-destructive tests (NDTs), pose risks of progressing into macro cracks, thereby compromising structural integrity and safety (Kannengießer & Böllinghaus, 2014), and may exacerbate the corrosion behaviour of welded components (Schobbert, Böllinghaus, & Wolf, 2003) (Stelling, et al., 2005). During a thermal cycle of laser welding, the cooling rate of metals after welding can exceed 1×10<sup>5</sup> K/s (Chande & Mazumder, 1984), and the cooling times is commonly in tens of milliseconds (Fotovvati, Wayne, Lewis, & Asadi, 2018). Additionally, in the mushy zone where the liquid and solid coexists, the solidification shrinkage, thermal contraction of the dendritic grains, as well as the surrounding restraint, accumulates strains in the liquid films at the trailing end of the weld pool, which increases the hot cracking susceptibility (Kou, Welding metallurgy, 2003) (Agarwal, 2019).

The occurrence of hot cracking is driven under complex interactions among the factors involving thermal, metallurgical, and mechanical aspects, influencing the restraint and the solidifying microstructure of the welded materials (Cross, 2005). In the metallurgical aspect, Pumphrey introduced the shrinkage-brittleness theory, stating that the ductility of the weld metal is low within a brittle temperature range (BTR) between the solidus and coherency temperature (Pumphrey, 1948), at which the solidifying dendrites form a rigid network and transmit stresses (Rappaz & Dantzig, 2009). Feurer described that if the rate of the residual liquid drawing back through the dendritic network by capillary flow is lower than the shrinkage rate, solidification cracks will occur (Feurer, 1977) (Manitsas & Anderson, 2018) (Lippold, 2015). Based on Feurer's criterion, Rappaz assumed that the thermal strain is limited to the coherent dendrite region and cracks initiate in the thin film region ahead of the coherent dendrite network (Rappaz, Drezet, & Gremaud, 1999). Kou proposed a model focusing on the grain boundaries and the liquid between the grains and assumed voids that initiate cracks, being formed when the net expansion of the intergranular space exceeds the liquid feeding (Kou, 2015). Regarding the mechanical factors that involve strain and stress conditions, as well as restraints in the microstructure, Pellini elucidated that if the tensile strain of an intergranular liquid film exceeds a critical value, the liquid film ruptures and leads to the occurrence of cracking. The amount of strain is determined by the time the liquid film persists, affected by the solidification range and the cooling rate during welding (Pellini, 1952) (Böllinghaus & Herold, 2005) (Agarwal, 2019). Prokhorov stated that the ductility of the mushy zone decreases during solidification in the BTR (Prokhorov, 1956) (Agarwal, 2019) (Wall & Benoit, 2023). In

order to forecast the maximum tolerable strain, both Prokhorov and Senda et al. established a ductility model, of which the maximum strain is where the rate of change of strain with temperature intercepts the brittle temperature range determined by the solidus and liquidus temperatures (Prokhorov, 1956) (Senda, Matsuda, & Takano, 1973). In respect to the stress condition, Fisher concluded that simultaneous nucleation of many fine pores will take place once the liquid is exposed to a sufficiently large negative pressure, referring as liquid rupture, and proposed equations to calculate the threshold fracture pressure for homogeneous pore nucleation (Fisher, 1948). Chihoski studied the stress condition following a moving weld pool and analyzed the mechanism of how the welding parameters vary the tensile or compressive stress in the trailing region of the welding pool (Chihoski, 1972). Through Sigmajig tests, Zacharia found the solidification cracking occurs if a tensile stress field exerts on the trailing end of the mushy zone (Zacharia, 1994), and maintaining the mushy zone in a compressive stress field can hinder the formation of solidification cracking (Coniglio & Cross, 2020).

This study focuses on the mitigation of hot cracking during laser welding. Laser welding is a joining method widely applied in the fabrication of metal, offering the advantages such as high travel speeds, low thermal distortion, and its potential of automatic processing ensures high precision and consistent weld quality (Ismail, Okamoto, Okada, & Uno, 2011) (Spina, Tricarico, Basile, & Sibillano, 2007) (Belhadj, Bessrour, Masse, Bouhafs, & Barrallier, 2010) (Kirchhoff, 2013) (Chen, Ackerson, & Molian, 2009) (Alvarez, et al., 2019) (Zhang, et al., 2021) (Keivanloo, Naffakh-Moosavy, & Miresmaeili, 2021) (Vâlsan, Bolocan, Burcă, & Crăciunescu, 2023) (Farid & Molian, 2000).

During the laser welding process, which commonly utilizes a Nd:YAG, CO<sub>2</sub> or fiber laser, a light source supplies sufficient thermal energy onto a small area to melt and fuse the material. For a typical Gaussian beam, the intensity distribution of intensity can be described by (eq.1) (Trapp, Rubenchik, Guss, & Matthews, 2017):

$$I = I_0 \exp\left(-\frac{2r^2}{\sigma^2}\right) \tag{eq.1}$$

In this equation, r is the distance to the central axis, and  $\sigma$  is the width where the intensity equals to  $\frac{1}{e^2}$  times of the peak intensity  $I_0$ .

The power density of a Gaussian beam follows the distribution described by (eq.2) (Muhammad, Daniel, Jean-François, & Dominique, 2010):

$$Q_{\nu} = Q_0 \exp\left(-\frac{3r^2}{r_c^2}\right) \tag{eq. 2}$$

in which Qv is the total volumetric heat flux in Wm<sup>-3</sup>,  $r_c$  is the flux distribution parameter for the cone as a function of z direction. r represents the distance to the central axis, calculated by (eq.3).

$$r = \sqrt{x^2 + y^2} \tag{eq. 3}$$

 $Q_0$  is the maximum heat flux, which can be derived from the thermal energy conservation rule in (eq.4),

$$\eta P = \int_{z_i}^{z_e} \int_0^{2\pi} \int_0^{r_c} Q_0 \exp\left(-\frac{3r^2}{r_c^2}\right) r dr d\theta dh \qquad (eq. 4)$$

in which  $\eta$  is the process efficiency,  $r_c$  represents the flux distribution parameter of the cone as a function of the depth, calculated in (eq.5),

$$r_c = \frac{r_i(r_e - r_i)(z - z_i)}{z_e - z_i}$$
 (eq. 5)

in which  $z_e$  is the upper z-coordinate and  $z_i$  is the lower z-coordinate of the cone,  $r_e$  is the lager radius of the cone, and  $r_i$  is the smaller radius of the cone.

The interaction between the laser beam and the steel sheet includes reflection, transmission, scattering and absorption. The absorption process transfers the laser power into thermal energy and heats up the material and affects the quality of welding. As an example, the increase of absorptivity contributes to localized heating and increases the efficiency of energy utilization and affects the thermal gradient across the weld zone that dominates the fluid flow dynamics and the solidification behaviour (Liao & Yu, 2007) (Xie, Kar, Rothenflue, & Latham, 1997) (Mahrle & Beyer, 2009) (Ren, Zhang, Fu, Jiang, & Zhao, 2021) (Yang, Bauereiß, Markl, & Körner, 2021). For a certain material and a certain incident angle of the laser beam, the absorptivity can be calculated by (eq.6) (Dausinger & Shen, 1993).

$$A = \frac{1}{2} \left( \frac{4n\sin(\alpha)}{(n^2 + k^2)\sin^2(\alpha) + 2n\sin(\alpha) + 1} + \frac{4n\sin(\alpha)}{n^2 + k^2 + 2n\sin(\alpha) + \sin^2(\alpha)} \right) (eq. 6)$$

The first term in this equation represents the polarization parallel to  $\alpha$ , and the latter term representing the polarization orthogonal to  $\alpha$ . The incident angle  $\alpha$  is defined as the angle between the beam and the welding direction at the upper surface of the sheet, as displayed in Fig. 2.2. n is the refraction index and k is the extinction index such that in the case of a metal at a wavelength  $\lambda_l \geq 0.5 \ \mu m$ , n and k follows the relation:

$$n^2 + k^2 \ge 1 \tag{eq.7}$$

Hence, as Fig. 1.1 shows, when the incident angle tilts away from  $90^{\circ}$ , the absorption rate will first slightly increase, then drop to 0 when the beam becomes parallel to the welding specimen. The angle where the maximum absorption rate is reached depends on the n land k value of the specific material.

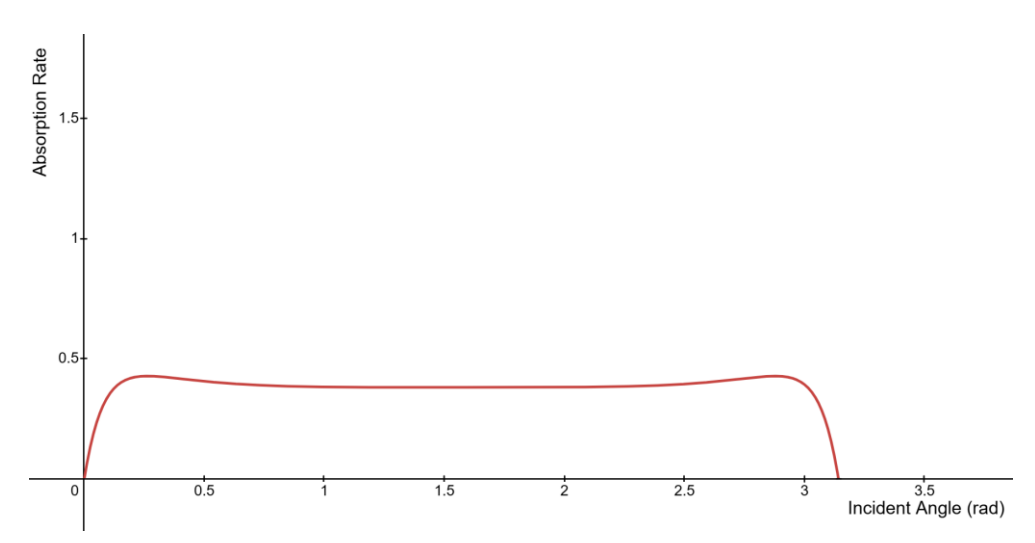


Fig. 1.1. Absorption rate of iron as a function of incident angle in the unit of radius, the wavelength of the incident beam is  $1.030 \mu m$ . Data retrieved from (Johnson & Christy, 1974).

According to the thermal energy on the welding site, the process can operate in two main modes: keyhole mode and conduction mode. As illustrated in Fig. 1.2 (a), in the case where the energy density is not sufficient to create a keyhole, the conduction of heat from the top surface to the inner part creates a weld pool, resulting in partial penetration. Such an operation mode is called conduction mode (Agarwal, 2019). As Fig. 1.2 (c) shows, when the energy density is sufficient to surpass the melting point and vaporize the material, the exerting recoil pressure on the surface of the melt pool causes the depression through the thickness, a keyhole is created (Trapp, Rubenchik, Guss, & Matthews, 2017) (Agarwal, 2019). Such a configuration enhances laser energy absorption, (Trapp, Rubenchik, Guss, & Matthews, 2017) as the laser beam is also able to reflect inside the keyhole (Liao & Yu, 2007) which benefits weld pool penetration (Lancaster, 1984) (Luo, et al., 2019). Furthermore, a transition mode shown in Fig. (b) exists when the energy density is increased in between the conduction mode and the keyhole mode. A shallow penetration is obtained by a keyhole, of which the ratio between the depth and width is around 1 (Kripalani & Jain, 2021).

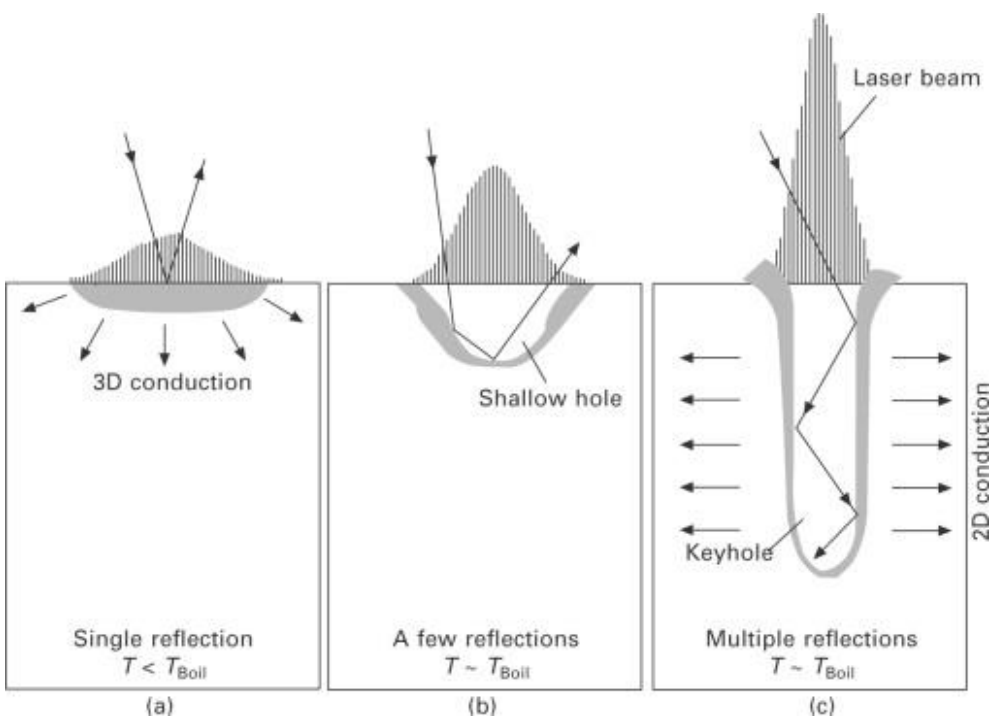


Fig. 1.2. Graphic illustration of (a) conduction mode, (b) transition mode (c) typical keyhole mode, T represents the temperature. Retrieved from (Miyamoto, 2013).

Since the solid material is melted during laser welding, complex flow fields are generated within the weld pool. The Marangoni effect is a key factor with radial symmetry (Fuhrich, Berger, & Hügel, 2001). Marangoni flows are driven by surface tension. If the coefficient of surface tension  $\gamma(r)$  reaches the maximum in the centerline as shown in Fig. 1.3 (a), the surface flow is driven towards the middle of the weld pool and flows to the bottom, then moves to the surface along the bottom of the weld pool. This flow transfers the heat to the bottom of the weld pool through convection, which enhances the melting and generates deeper weld pools (Fuhrich, Berger, & Hügel, 2001). If the coefficient of surface reaches a minimum at the centerline as shown in Fig. 1.3 (b), the surface fluid flows towards the outer boundaries, and the consequential convection transfers heat to the outer boundaries (Fuhrich, Berger, & Hügel, 2001).

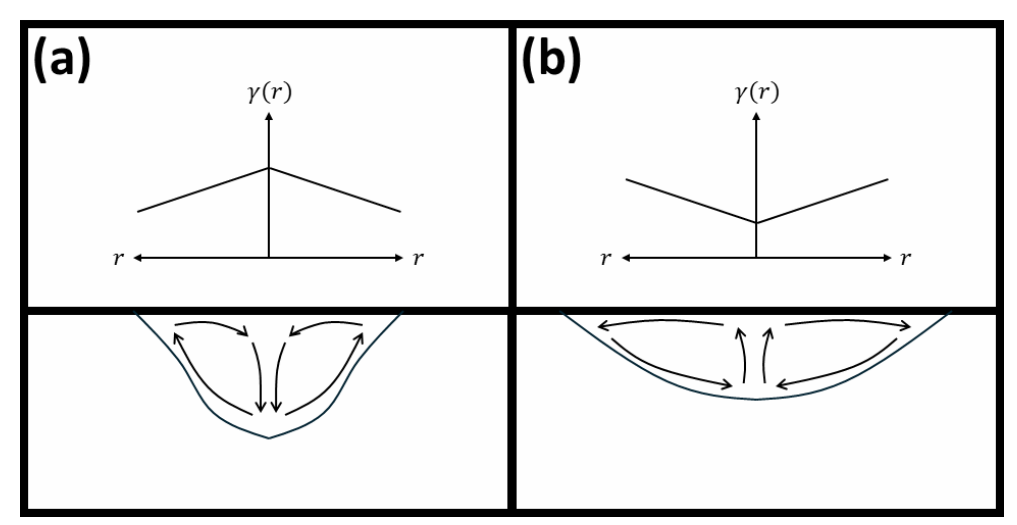


Fig. 1.3. Schematic view of Marangoni flow developed in the weld pool when (a)  $\gamma(r)$  reaches maximum in the centerline, (b)  $\gamma(r)$  reaches minimum in the centerline. Reproduced from (Fuhrich, Berger, & Hügel, 2001)

The conditions of the welding process and the material properties dominate the postwelding microstructure of the welding zone, and the consequential morphology of the grains has a significant impact on the hot cracking susceptibility of the metal sheets. If these conditions result in finer grains, more grain boundaries are present, and the strain is partitioned over these grain boundaries causing a reduction in local strain. This prevents the liquid films present from rupturing (Böllinghaus & Herold, 2005) (Pellini, 1952). During the solidification process two metallurgical parameters, the thermal gradient (G) and the solidification rate (R) which describes the growing speed of the solid-liquid interface are the two key factors that affect the grain morphology (Schempp, et al., 2014). At a typical solidification condition, the value of G ranges from 100 to 1000 K·m<sup>-1</sup> (Kou, Welding metallurgy, 2003). Throughout the solidification process, R increases from the initial stage when the solidification starts at the fusion zone boundary to the final stage at the centerline whereas G decreases. As shown in Fig. 1.4, G/R determines the grain morphology, and G×R, that reflects the cooling rate, determines the grain size (Lei, et al., 2023). As the ratio of G/R decreases, the grain morphology transforms from planar to cellular, then to columnar, and eventually to equiaxed (Schempp, et al., 2014). In addition, a higher G×R value that indicates a higher cooling rate corresponds to a fine microstructure, while a lower G×R value corresponds to a coarser structure (Lei, et al., 2023).

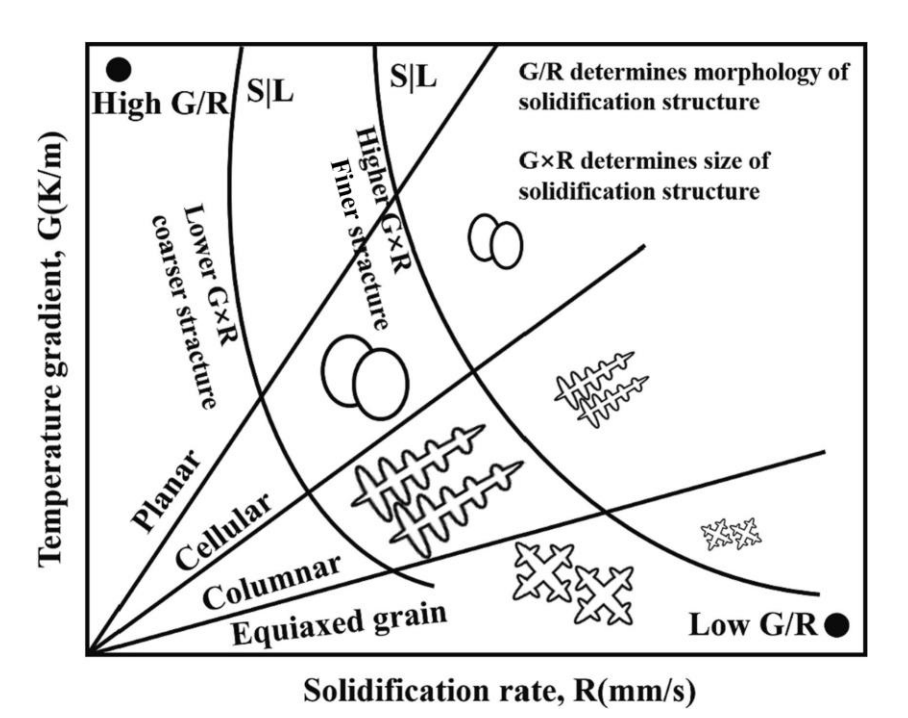


Fig. 1.4. Influence of the factors G and R on grain morphology. Retrieved from (Lei, et al., 2023).

In order to mitigate the hot cracking susceptibility during laser welding, various studies proposed different treatments in order to interfere with the conditions that cause hot Grain size reduction reduced the strain partitioned per grain boundary, preventing the rupture of liquid films present between the grains (Böllinghaus & Herold, 2005) (Pellini, 1952). To realize this, Yao et al. introduced external ultrasonic vibration to generate cavitation bubbles that aids grain refinement, as well the consequential thermal mixing decreases the temperature gradient, promoting the formation of equiaxed grains (Yao, Wang, Chen, Sui, & Yao, 2022). Li et al. utilized an oscillating beam for laser welding and found the grains are refined due to a lower thermal gradient and less stress concentration (Li, Mi, & Wang, 2020). In the aspect of monitoring the local temperature gradient, Schaefer et al. studied the adjustment method of a sinusoidal laser and found that a larger difference between the amplitude and the average power generates shorter cumulated cracks (Schaefer M., Kessler, Scheible, & Graf, 2017). It is also found that increasing the frequency between two adjacent power peaks acts as a pre- and pos-welding treatment, that contributes to the liquid back filling process which could heal the cracks (Pakniat, Ghanini, & Torkamany, 2016). Schaefer et al. added a trailing low power laser spot following the original spot that extends the solidification time (Schaefer M., Kessler, Scheible, Speker, & Harrer, 2017). Bertrand et al. examined the effect of the shape of the pulse when applying a pulsed laser beam on metal (Bertrand & Poulon-Quintin, 2015). Bertrand et al. stated that the alloys with lower reflectivity are more prone to the input energy with a steep slope, and slowly rising input energy is more preferrable for alloys with higher reflectivity (Bertrand & Poulon-Quintin, 2015). In regard of the elemental and microstructural aspect on hot cracking, Shih (Shih, 2013), Wang et al. (Wang J., et al.,

2022) studied the relation between different elements and hot cracking. Kim et al. highlighted the significance of microstructure modulation in mitigating hot cracking tendencies (Kim & Nam, 1996).

For providing qualified or quantified measurements of the hot cracking susceptibility of the materials during welding, various test methods have been developed. These test methods can be categorized into intrinsic and extrinsic tests (Wall & Benoit, 2023). Intrinsic tests provide qualified results by utilizing simpler and capable testing facilities to, which is less expensive (Wall & Benoit, 2023) (Kannengießer & Böllinghaus, 2014). Extrinsic tests measure with controllable external loads exerting on the specimens, which are generally more expensive and of higher complexity, but ensuring the ability to quantify the hot cracking susceptibility (Wall & Benoit, 2023). Free edges tests are applied in this study, which will be detailed in Chapter 2.

Among the strategies for mitigating the hot cracking susceptibility, the field of beam shaping still lacks investigation. This study focuses on exploring the effect of varying different welding conditions, including controlling the welding speed to vary the heat input, adjusting the beam spot diameter by defocusing and changing the incident angle of the beams by tilting the laser head for welding TRIP steel sheets. High-speed camera and welding cameras are applied to film the welding behavior of plumes and fluid flows to reveal the keyhole and fluid behavior during welding processes. Thermal couples are also attached to the samples during welding to record the transverse temperature data and provide information of thermal fields. The characterization macrostructures and elemental analysis are conducted by optical microscope and SEM-EDS technique. A free-edge welding test is utilized to quantify the resulting hot cracking susceptibility, in order to make comparisons and summarize proper strategies for providing crack-free TRIP steel sheets.

## 2 Experimental

For the purpose of characterizing the hot cracking susceptibility, the free edge test, as an intrinsic test that makes use of self-restraint, is selected for the experimental work (Wall & Benoit, 2023).

During free edge tests, the laser beam moves at a certain distance parallel to the free edge while the other edge is clamped, as shown in Fig. 2.1. The transverse restraint stress increases as the amount of the material around the welding line increases, i.e., with increasing distance from the free edge. The local heat source creates a melt pool and thermal gradients in the welded sample. The low temperature regions exert restraint on the elevated temperature region and hinder the shrinkage of the metal in the welding seam, which generates transverse tensile stresses (Wang D., et al., 2024). The restraint is constantly dictated by the distance of the welding beam from the edge and increases as the beam is positioned further away from the edge. Because of the consistent restraint condition, a hot crack will propagate through the width of the sample once it is generated, which is convenient to observe. At a certain critical distance where the difference between the restraint stress and the shrinkage tensile stress is lower than the critical cracking stress, no hot cracking of the samples will occur (Wang D., et al., 2024) (Coniglio & Cross, Towards Establishment of Weldability Testing Standards for Solidification Cracking, 2016) (Agarwal, 2019). Hence, the occurrence of the crack generated by the laser welding process can be regarded as an intuitive parameter to characterize the hot cracking susceptibility (Kannengießer & Böllinghaus, 2014). Additionally, to discover the thermal behavior under different welding conditions, three groups of thermocouples are attached to the steel sheet 1mm, 2mm, and 3mm from the centerline towards the clamped edge to conduct in-situ temperature measurements. The diameter of a K-type thermocouple is 0.25 mm and is placed 10 mm from the entrance of the plate, as shwon in Fig. 2.1 (b).

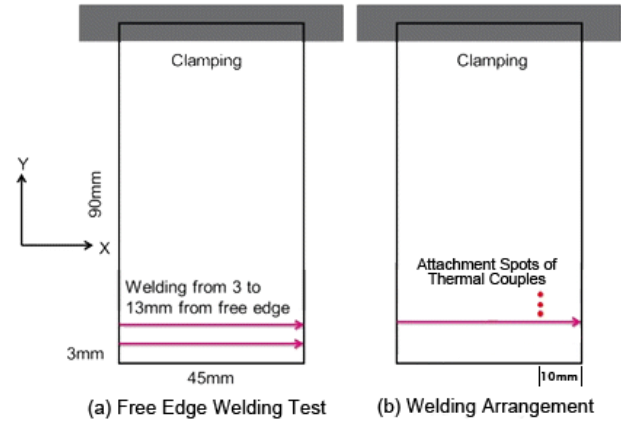


Fig. 2.1. Schematic of the experimental arrangement of a free edge welding test.

Laser beam is employed on rectangular Al-Rich TRIP sheets provided by TATA Steel Europe with dimension  $90 \times 45 \text{mm}^2$  and a thickness of 1.5 mm. The steel sheets are coated

with a zinc layer. The chemical composition of the Al-rich TRIP steel used in the experiments is listed in Table 2.1.

As a type of AHSS, TRIP steel enhances its strength and ductility by utilizing transformation induced plasticity effect, in which the retained austenite within the ferrite matrices transforms into martensite when undergoing plastic deformation and strain is applied (Soleimani, Kalhor, & Mirzadeh, 2020) (Liu, He, & Huang, 2018) (Jacques, 2004) (Timokhina, Hodgson, & Pereloma, 2004) (Ficher, et al., 2000).

It is worth noticing that the carbon (Z=6) content, which is added for stabilizing the austenite (Soleimani, Kalhor, & Mirzadeh, 2020), is not detected because it produces X-ray in longer wavelength which is easier to be trapped in the material, and it is also difficult to distinguish this signal from that arising from the surface contamination (Konopka, 2013). In the production of TRIP steels, the addition of Si and Al can inhibit the formation of carbides and cementite and benefits the carbon enrichment in austenite, and promote the formation of ferrite and bainite (Takahashi & Bhadeshia, 1991) (Jacques, 2004) (Jacques, et al., 2001) (Girault, et al., 2001). Mn increases the ductility and impact energy at low temperature (Lee, et al., 2014) and stabilizes the austenite (Sugimoto, Usui, Kobayashi, & Hashimoto, 1992) (Baik, Kim, Jin, & Kwon, 2001).

Table 2.1. Semi-quantitative elemental composition of the TRIP steel sample analyzed by scanning electron microscopy and energy dispersive X-ray spectroscopy (SEM-EDS).

Element	Fe	Al	Si	Mn
Composition (wt.%)	96.905±0.13	$0.690\pm0.02$	$0.265\pm0.02$	2.135±0.04

For the welding experiments, a Trumpth Nd: YAG TruDisk laser with a wavelength of 1030 nm, a full focusing angle of  $6.1^{\circ}$ , a Rayleigh length of 2.813 mm, and focal distance of 223 mm is used. The waist width  $w_0$  of the generated Gaussian beam is 0.2 mm, and it is selected as the narrowest beam spot diameter for the experiments. By defocusing the beam spot size can be increased. In the experiments the laser head is stationary, and the workpiece is moved underneath.

To investigate the effect of the shape of the laser beam on hot cracking susceptibility, three welding parameters are studied, i.e. the travel speed of the beam, the spot diameter and the incident angle of the beam. Table 2.2 lists parameters employed.

The laser power is P maintained at 4 kW for all experiments, including the distance from free edge 13 mm to observe the appearance of typical welds, and the distance of 10 mm when measuring the transverse temperature. In the table the calculated heat input is added, defined by dividing the input power by the spot area, assuming a process efficiency  $\eta$  of 1.

Based on the experiments with an incident angle of 90° with varying spot sizes it was decided to continue the experimental work on the variation of the incident angle with a spot diameter of 0.6 mm. The laser head is first tilted within the plane parallel to the welding direction where the tilting angle is defined as shown in Fig. 2.2. and Fig. 2.3. The

duration of the welding process of the sheet size indicated is  $1.184 \, s$ ,  $1.125 \, s$  and  $0.844 \, s$ , corresponding to the travel speed of  $32 \, mm/s$ ,  $40 \, mm/s$  and  $53.33 \, mm/s$ .

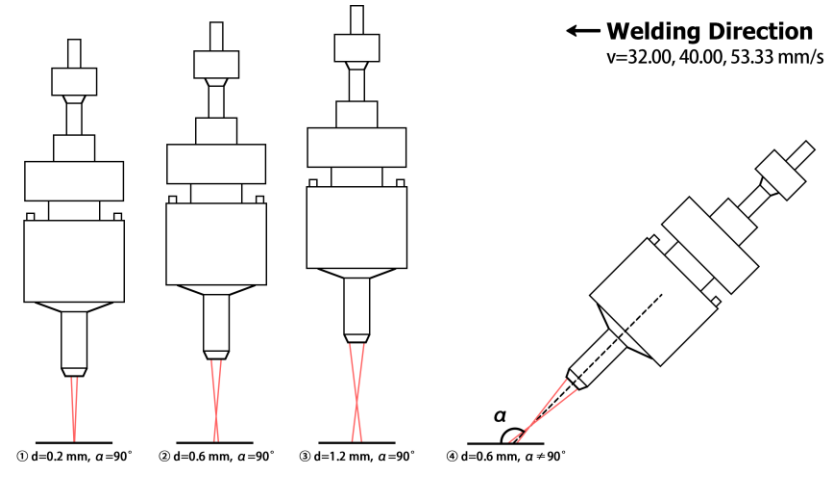


Fig. 2.2. Schematic of experimental arrangement.

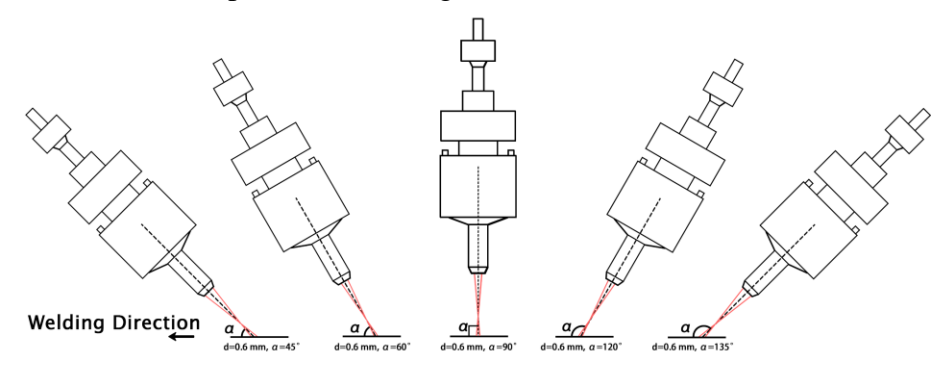


Fig. 2.3. Schematic of the test arrangement regarding to different incident angles.

Table 2.2. Diameter of beam spots and incident angles selected for free edge tests and the corresponding areas of beam spots, welding travel speed and heat input, maintaining a laser power of 4 kW and a wavelength of 1030 nm.

No.	Spot Diameter (d) (mm)	Incident Angle (α) (°)	Welding Speed (v) (mm/s)	Spot Area (A) (mm <sup>2</sup> )	Heat Input (J/mm)
1	0.2	90	40	0.031	100
2			32		125
3		90	40	0.283	100
4			53.33		75
5	0.6	60	40	0.330	100
6		120	40	0.550	100
7		45	40	0.377	100
8		135	40	0.377	100
9	1.2	90	40	1.131	100

For observing the interaction between the laser and the steel sheet, the motion of the welding process is filmed by a Phantom® MIRO M310 high speed camera from the free edge side, with an exposure time of 36 µs and a frame rate (FPS) of 400 Hz. To observe the condition of the keyhole and the solidification behavior of the mushy zone, a Cavitar® VCXG-15M camera is fixed to the laser head to record the motion around the keyhole at an FPS of 100 Hz. A hairdryer is placed near the laser spot to blow away the vapor and dust that hinder observations, as depicted in Fig. 2.4.

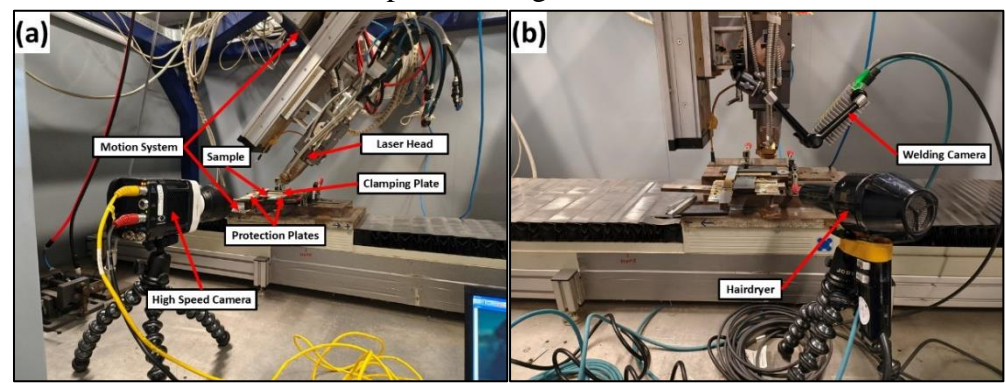


Fig. 2.4. The experimental setup when observing by (a) Phantom® MIRO M310 high speed camera, (b) Cavitar® camera.

The welded samples are ground, polished and then etched in 2% Nital composed of 2% concentrated nitric acid and 98% ethanol (De, Speer, & Matlock, 2003) and LePera etchant, which is composed of 1% sodium metabisulfite aqueous solution and 4% picric acid ethyl alcohol solution in 1:1 ratio (LePera, 1979).

A KEYENCE® VHX-7000 digital microscope is used to characterize the microstructure, and a JEOL JEM-IT-100 SEM is applied for providing EDS analysis under 20.0 kV acceleration voltage to give information about the semi-quantitative elemental composition of the samples.

The measurement of the top and bottom width are performed by stitching the bead with optical microscope and calculating the average fusion zone widths from 10 randomly selected sites, as shown in Fig. 2.5. The range of the fusion zone is determined within the outer boundaries of the undercut, and the length of the weld pool is measured as the length of the depressed region located at the end of the bead.

The measurement method of the waist, defined as the narrowest width of the fusion zone in the cross section, and the surface-to-waist distance is defined as the distance from the top surface to the plane where the waist is located are shown in Fig. 2.6.



Fig. 2.5. Measurement of the width of the top surface of the bead welded by a welding process with a 4 kW Nd: YAG laser beam with a 1030 nm wavelength, a beam spot diameter of 0.6 mm, an incident angle of 90° and a travel speed of 53.33 mm/s.

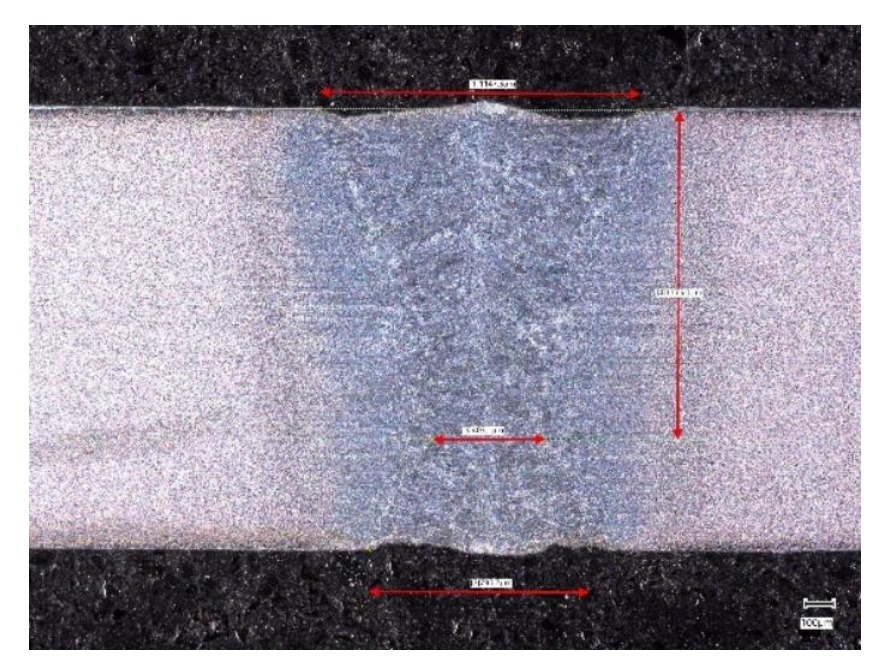


Fig. 2.6. Measurement of the waist width and surface-to-waist distance of the fusion zone welded by a welding process with a 4 kW Nd: YAG laser beam with a 1030 nm wavelength, a beam spot diameter of 0.2 mm, an incident angle of  $90^{\circ}$  and a travel speed of 40 mm/s. The top and bottom width is not adopted because the values are already measured by the method shown in Fig. 2.5.

### 3 Results

In this chapter, the effect of the processing parameters on the bead dimensions and the behavior of the melt pool during welding are characterized by utilizing high speed cameras and digital microscopes, and the hot cracking susceptibility is then qualified by free-edge welding tests.

### 3.1 Impact of Welding Speed

The speed of a welding process dominates the heat input and affects thermal behavior such as the cooling rate and thermal gradient. It also affects the geometry of the weld pool and leads to different impacts on hot cracking susceptibility which is material dependent (Zhang, et al., 2021) (Keivanloo, Naffakh-Moosavy, & Miresmaeili, 2021) (Zhu, Liu, Gou, Gao, & Chen, 2021) (Wang D. , et al., 2024). As listed in Table 3.1, the tests investigating the effect of different travel speeds involved three values: 32.00, 40.00 and 53.33 mm/s, corresponding to a heat input of 75, 100 and 125 J/mm, respectively. According to Johnson et al., the absorption rate of iron for an incident angle  $\alpha$ =90° and a wavelength  $\lambda$ =1030 nm is 0.38179 (Johnson & Christy, 1974).

Table 3.1. and Figs. 3.1-3.3. Welding appearance of beads and melt pool generated by a 4 kW Nd: YAG laser with 1030 nm wavelength, an incident angle of 90° and a spot diameter of 0.6 mm for different travel speeds. The scale bar represents for 1 mm.

		1
Welding Speed (mm/s)	Heat Input (J/mm)	Weld Appearance
32.00	125	
40.00	100	
53.33	75	

The profiles of the bead widths together with standard deviations are plotted in Fig. 3.4. As the travel speed increases and the heat input decreases, the bead becomes narrower as less metal is molten by the reduced heat per unit length of weld. In addition, the standard deviation of the width also decreases as travel speed increases, indicating that an elevated heat input, i.e. lower travel speed, causes a more perturbated turbulence in the fluid flow.

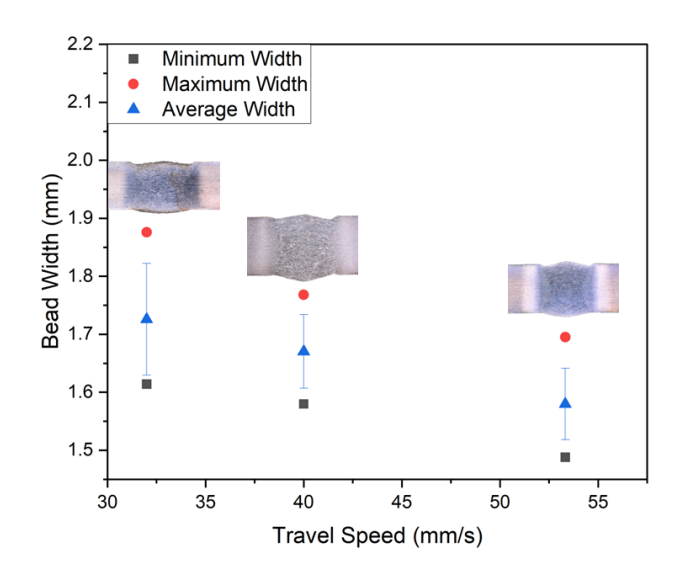


Fig. 3.4. Width of the weld beads generated as a function of travel speeds for a 4 kW Nd: YAG laser with 1030 nm wavelength, a spot diameter of 0.6 mm and an incident angle of 90°.

The still frames, displayed in Fig t4. (a)-(c), reflect the welding progress for different heat input by welding with different travel speeds. When the heat input increases, most of the plume tends to be prone to exit from the bottom surface since more heat is delivered to the bottom of the melt pool and aids melting the metal at the bottom. Hence, in the case when the amount of plume ejecting from the top, the absorption of laser power induced by the plasma clouds will also reduce the effective power delivered to the top surface and lower the surface power density.

As illustrated in Fig. 3.5 (d)-(f) and Fig. 3.6, all laser beams for the three travel speeds create catenoid keyholes, and the geometrical dimensions of the keyhole increase as heat input increases, as the metal absorbs more heat and melts. The line occurred in the middle of Fig. 3.5(e) is inferred to be the segregation line during fabrication of the TRIP sheet.

It is also seen from Fig. 3.6 (b) that, as the travel speed is increased to 53.33 mm/s, the ejection angle of the plume slightly tilted to 87°, however, a 3° tilting does not reduce laser beam absorption by the plume significantly and therefore does not extend the melt pool length. The longest melt pool length is 7.56 mm, generated when v equals 32 mm/s, in this case, the heat input is 125 J/mm, and the solidification time is extended.

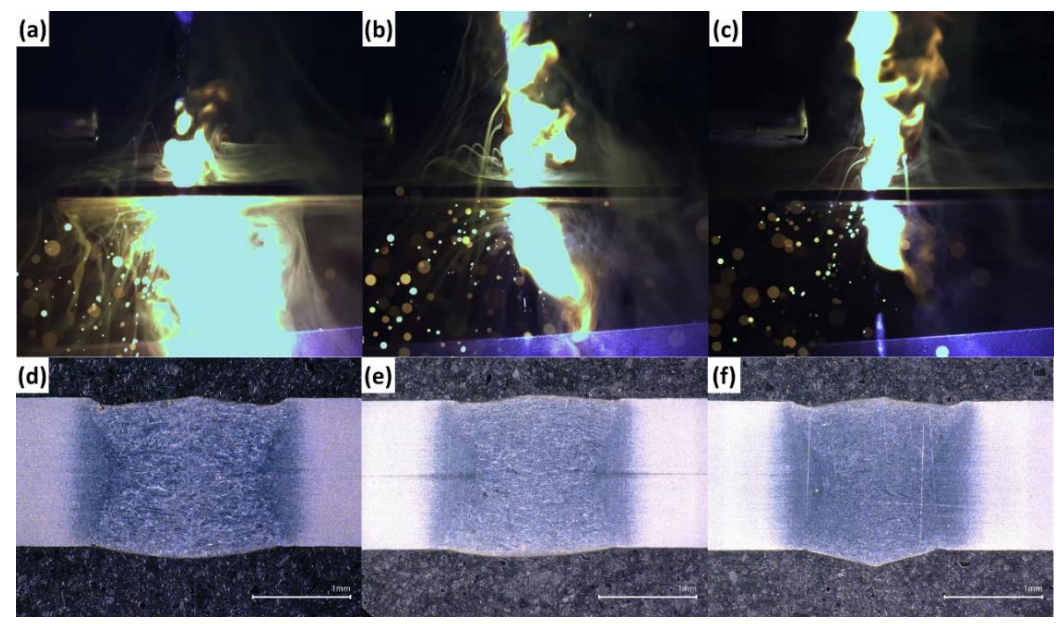


Fig. 3.5. Still images during the welding process showing the plasma plume ejection with a travel speed v of (a) 32.00 mm/s, (b) 40.00 mm/s, (c) 53.33 mm/s and the corresponding cross section microstructure when v equals to (d) 32.00 mm/s, (e) 40.00 mm/s, (f) 53.33 mm/s for a 4 kW Nd: YAG laser with 1030 nm wavelength, a 0.6 beam spot size, and an incident angle of 90°.

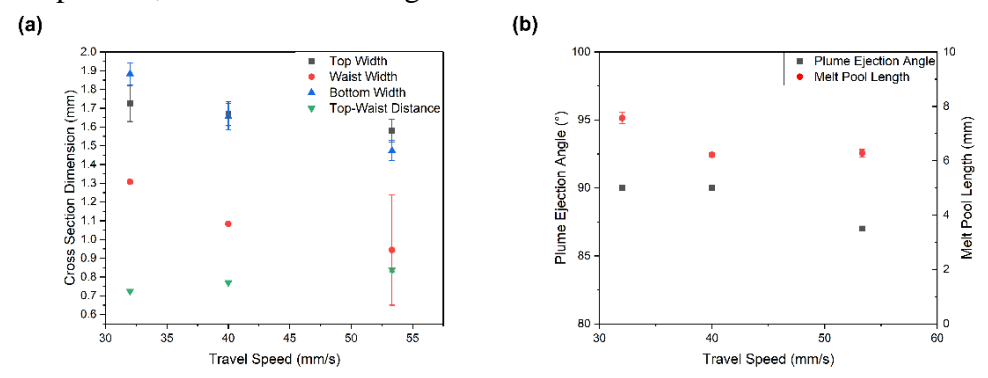


Fig. 3.6. (a) Geometrical parameters of the cross section of the bead, (b) Length of the melt pool and the plume ejection angle as a function of travel speed.

#### 3.2 Impact of Beam Spot Diameter

The experiments to study the effect of the beam shaping on the welding process of TRIP steel sheets were then performed by defocusing the beam to produce different spot diameters. For the experiments listed in Table 3.2, the incident angle is maintained at 90°, and the travel speed is set at 40 mm/s, at a laser power 4 kW, keeping the heat input at 100 J/mm. The power density delivered to the surface is reduced as the diameter of the beam increases from 0.2 mm to 1.2 mm.

Table 3.2. and Figs. 3.7-3.9. Welding appearance of the bead and melt pool generated by a 4 kW Nd: YAG laser with 1030 nm wavelength, an incident angle of  $90^{\circ}$  and a travel speed of 40 mm/s in various spot diameters. The length of the scale bars in the pictures are 1 mm.

Spot Diameter (mm)	Spot Area (mm <sup>2</sup> )	Welding Appearance
0.2	0.031	Market Andrew Control of the Control
0.6	0.283	
1.2	1.131	

The dimensions of the weld pool generated are plotted in Fig. 3.10. The length of the melt pool generated by a laser beam with a diameter of 0.2 mm is 3.25 mm, while the melt pool generated by a beam with a diameter of 0.6 mm is 6.22 mm long. Delivering the most dispersed energy density, the beam with a diameter of 1.2 mm generates a melt pool with a length of 4.95 mm.

Higher power density leads to concentrated power dissipation, and the formation of a keyhole. It can be observed from Fig. 3.11(a) that the laser beam fully penetrates the sheet, and the power absorption rate of the material surrounding the spot is lower than the case when the diameter is defocused to 0.6 mm. The area of the spot with 1.2 mm diameter is four times larger than the area of the spot with 0.6 mm diameter, therefore less power is dissipated to per unit area of surface due to the lower power density and less metal is melted. A keyhole is not formed, and the process operates in conduction mode. Heat dissipation in the workpiece increases.

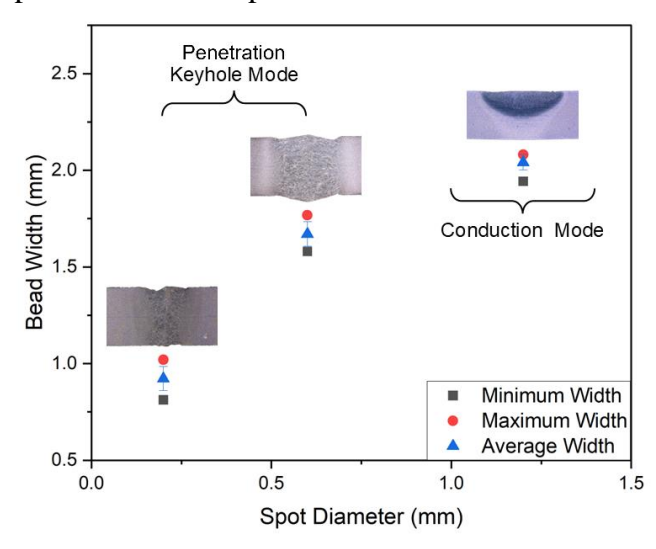


Fig. 3.10 Bead width as a function of spot diameter for a 4 kW Nd: YAG laser beam with a 1030 nm wavelength, an incident angle of 90° and a travel speed of 40 mm/s.

The still frames representing the welding process for different beam sizes are displayed in Fig. 3.11(a)-(c). The ejection paths of the plasma plumes are all perpendicular to the direction of welding. When the laser beam is at the focal point such that the spot diameter is 0.2 mm, most of the plume ejects from the bottom, along with severe spattering, which implies that much of the power is wasted (Khan, et al., 2022). As a reference, the energy loss through the keyhole during laser welding of zinc coated steels is estimated to be around 40% (Pan, 2011). As the spot diameter increases, the plume ejects more from the top surface and less from the bottom, it is worth noticing that the plasma cloud above the surface can absorb the laser energy (Schaefer M., Kessler, Scheible, Speker, & Harrer, 2017). It is estimated that the energy loss combined with losses by reflection, radiation and convection is around 8% (Pan, 2011). When the spot diameter is expanded to 1.2 mm, the plume only exits from the top surface, indicating that the welding mode switched from keyhole mode to conduction mode. The corresponding cross section macrostructures of the fusion zones are displayed in Fig. 3.11(d)-(f), and the dimensions measured are plotted in Fig. 3.12. It is indicated that the most concentrated heat source of 0.2 mm spot diameter penetrates the steel sheet fully, resulting in a thinnest catenoid keyhole, where the top width is 0.92 mm, the bottom width is 0.88 mm, and the waist, where the keyhole is the narrowest, is 0.50 mm wide, located a distance from the surface of 0.93 mm. The plasma plume in the welding process where the spot diameter is increased to 0.6 mm ejects from both surfaces of the steel sheet, as shown in Fig. 3.11(b), the open keyhole is corroborated in the microstructure in Fig. 3.11(h). The top width is now 1.67 mm, the bottom width is 1.66 mm, and the waist is 1.08 mm wide, located 0.771 mm below the top surface. The increasing standard deviation of the waist width with spot diameter indicated the extent of turbulence caused by the collision of the fluid flow in the melt pool (Ai, et al., 2018) (Xue, et al., 2022). Compared to the laser with 0.6 mm size that creates a symmetric catenoid keyhole, the laser of 0.2 mm size passes through the keyhole with a lower absorption rate compared to the defocused beams. The laser with 1.2 mm spot diameter generates a wider bead but lacks penetration, because of the laterally dissipated power. It can be seen that the columnar grains grow towards the top surface in a region  $\pm 0.63$  mm from the centerline, which corresponds to the region where the laser impinges on. As the growth direction of the grains represents the highest thermal gradient (Liang, 2024), it is inferred that the laser power is dissipated on the surface instead of penetrated deeply into the weld pool in this case, i.e. conduction mode.

As shown in Fig. 3.11 (d)-(f), the extent of deformation of the top surface decreases as the beam size increases, due to the reduced recoil pressure generated during the vaporization of surface metal (Kumar, Mukherjee, & Bandyopadhyay, 2017). A concentrated heated area undergoes more vaporization associated with a higher recoil pressure.

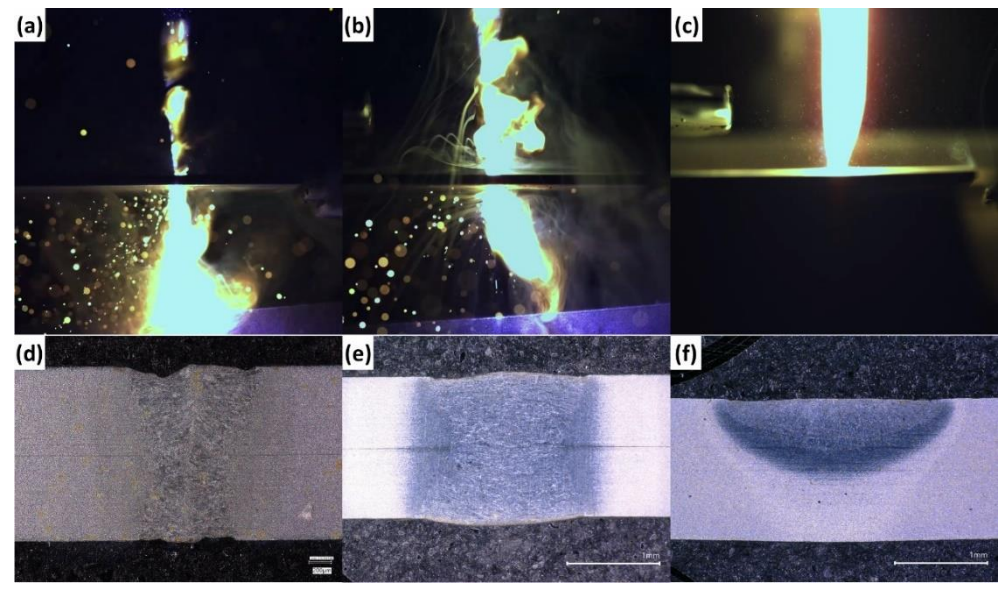


Fig. 3.11. Still frames during the welding process showing the plasma plume ejection with a beam spot diameter d of (a) 0.2 mm, (b) 0.6 mm, (c) 1.2 mm and the corresponding cross section macrostructure when d equals to (d) 0.2 mm, (e) 0.6 mm, (f) 1.2 mm at a 4 kW Nd: YAG laser beam with a 1030 nm wavelength, an incident angle of 90° and a travel speed of 40 mm/s.

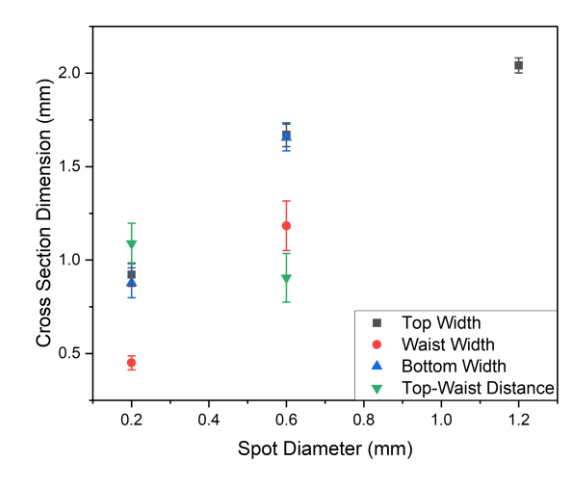


Fig. 3.12. Dimensions of the cross section of the bead corresponding to different spot diameters for a 4 kW Nd: YAG laser with 1030 nm wavelength, an incident angle of 90° and a travel speed of 40 mm/s.

Among the three beam spot diameters evaluated in the experiment, a diameter of 0.6 mm will ensure full penetration, and less power is lost. The experimental investigation on the influence of the incident angle on the welding process was conducted with a constant spot diameter of 0.6 mm.

#### 3.3 Impact of Incident Angle in Longitudinal Direction

The adjustment in the incident angle of the laser beam influences the power density distribution and dissipation along the longitudinal direction. In addition, as displayed in Fig. 3.13, a tilted laser beam supplies more power onto the walls of the keyhole and affects the behavior of molten fluid flow within the melt pool (Kumar, Mukherjee, & Bandyopadhyay, 2017) (Khan, et al., 2022). To maintain a constant beam width in transverse direction, the object distance, defined as the distance between the top surface of the steel sheets and the laser optics for the experiments studying the interaction of the laser beam with different incident angles are equivalent to the case when a diameter of d=0.6 mm is applied at an incident angle of 90°. The travel speed is maintained at 40 mm/s to ensure the heat input stays at 100 J/mm. Table 3.3 provides an overview of the incident angle applied, the calculated spot diameter and the resulting appearance of the laser beads.

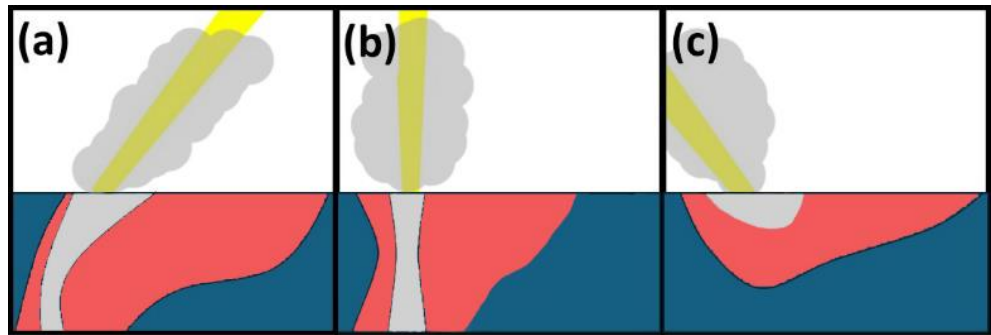


Fig. 3.13. Schematic illustration of the weld pool when the incident angle (a)  $\alpha > 90^{\circ}$ , (b)  $\alpha = 90^{\circ}$ , (c)  $\alpha < 90^{\circ}$ .

The Fresnel equation of absorptivity (eq.6) states that the absorptivity of laser energy changes with varying incident angles. According to Johnson et al., at a wavelength of 1030 nm, n equals to 2.9421 and k equals to 3.9094 for iron (Johnson & Christy, 1974). The absorptivity values of iron as a function of incident angles are listed in Table 3.3 as well.

Table 3.3. Fig. 3.14-3.18. Welding appearance of the bead and melt pool generated by a 4 kW Nd: YAG laser with 1030 nm wavelength, a spot diameter of 0.6 mm and a travel speed of 40 mm/s in various incident angles. The length of the scale bar represents 1 mm.

Incident Angle	Major Axis (mm)	Absorptivity (Fe)	Welding Appearance
45°	0.8	0.38836	
60°	0.7	0.38296	
90°	0.6	0.38179	
120°	0.7	0.38296	
135°	0.8	0.38836	

Among the five welding samples, the welding process by laser beams with incident angles of  $45^{\circ}$  and  $60^{\circ}$  are observed to cause the least spattering, while the welding process involving a beam of an incident angle of  $135^{\circ}$ , caused the most severe spattering. This observation of the spattering phenomenon is also reflected in Fig. 3.19 where the standard deviation in the width of the wave-like fusion line is the largest, referring to a more erratic process.

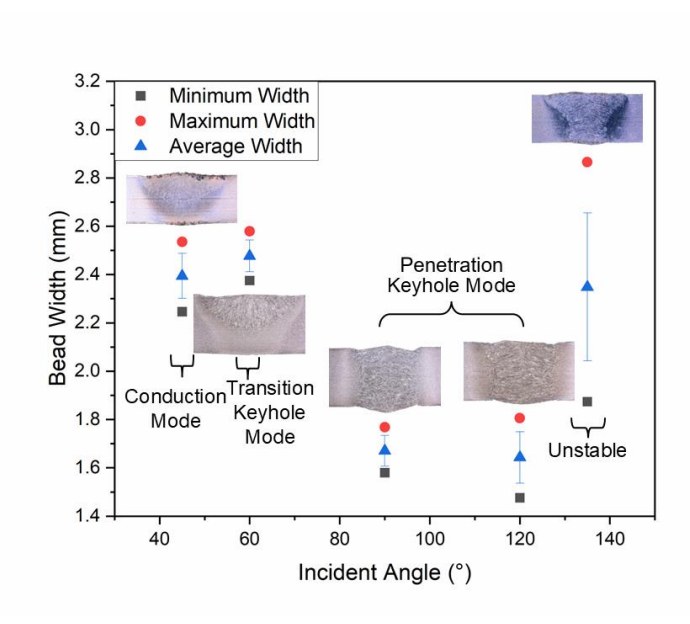


Fig. 3.19. Dimensions of the bead width as a function of the incident angle for a 4 kW Nd: YAG laser with 1030 nm wavelength, a spot diameter of 0.6 mm and a travel speed of 40 mm/s.

As shown in Fig. 3.20 (a), when the incident angle  $\alpha$  is equal to 45°, the vapor and plasma are ejected vertically from the top surface and no plumes are observed at the bottom surface, indicating a conduction mode. When the incident angle is tilted to 60°, the angle of the plume ejection is inclined to around 60° as well, showing the starting of a transition keyhole mode that the inclined front wall changes the ejection angle of the plume, (Khan, et al., 2022) and the plasma cloud above the surface will cause absorption of the laser power. It can be concluded that the recoil pressure generated by a laser beam that  $\alpha$ =45° is not sufficient that it remains in conduction mode. The fusion zone displayed in Fig. 3.20(f)-(g) also indicated that the laser does not fully penetrate the steel sheet when the incident angle equals 45° and 60°, and the columnar grains grow in the direction towards the centerline of the bead along the maximum temperature gradient. As the incident angle increases, full penetration is achieved. The still frame Fig. 3.20(c) showed that the plasma plume ejects from both surfaces of the steel sheets, the open keyhole indicating a penetration keyhole mode is corroborated in the microstructure in Fig. 3.20(h), where the fusion zone showed a catenoid shape with a difference between the average top and bottom widths less than 0.88%. This is the lowest among all angles that achieve full penetration, as displayed in Fig. 3.23. For these configurations, the epitaxial columnar grains grow in the direction towards both the top and bottom surface centerline of the bead. As the incident angle tilts beyond 90°, the keyhole distorts more severely. In Fig 1(d) where  $\alpha$  is tilted to 120°, an open keyhole is maintained and the majority of vapor and plasma plume exit the top, while a smaller plume exits from the bottom surface at an angle of 120°.

As displayed in Fig. 1.1(h)-(j), compared to the keyhole generated by a 90° impinging laser beam, the keyholes generated by 120° and 135° incident angles have a narrower bottom width, and the waists are also further away from the top surface. Especially for the keyhole generated by an 135° incident angle, a distinction is observed between the keyhole top and root. It can also be seen that the undercut, which is the depressing occurring at the edge of the fusion zone, is most severe when welding at incident angles of 90° and 120°.

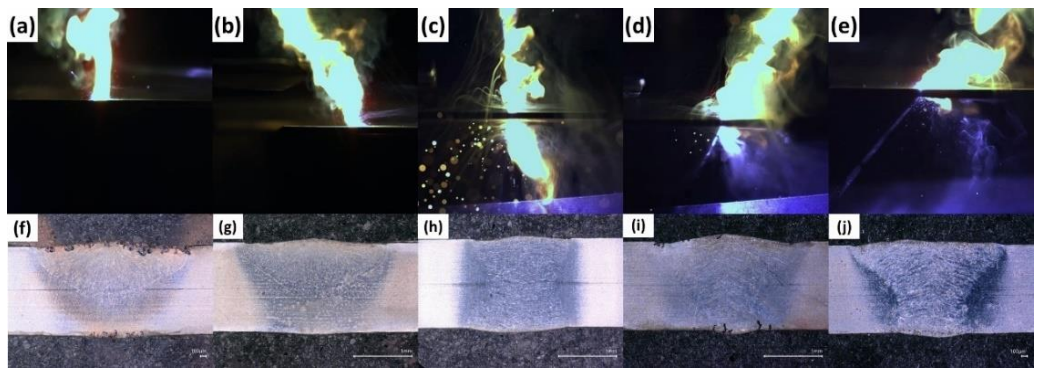


Fig. 3.20. Still frames during the welding process showing the plasma plume ejection with an incident angle  $\alpha$  of (a) 45°, (b) 60°, (c) 90°, (d) 120°, (e) 135° and the corresponding cross section macrostructure when  $\alpha$  equals to (f) 45°, (g) 60°, (h) 90°, (i) 120°, (j) 135° for a 4 kW Nd: YAG laser with 1030 nm wavelength, 0.6 mm spot diameter and a travel speed of 40 mm/s.

When the incident angle  $\alpha$  is tilted to 135°, the keyhole turns to be erratic, presenting a cyclical opening and closing behavior. As Fig. 3.21(a)-(d) shows, when the laser beam impinges on the top surface at the start of the welding process, the keyhole is closed, and the plume ejects only from the top surface with an  $100^{\circ}$ - $105^{\circ}$  angle. After a brief period of time, the keyhole opens at the bottom and the plume shortly ejects from the bottom vertically for 7.5 milliseconds on average, after which the keyhole at the bottom surface closes again, and the ejection angle of the plume is enlarged. In the last step, the keyhole bottom opens permanently with most of the plume ejecting from the top surface at an angle of around  $135^{\circ}$ , while a small portion of the plume ejects from the bottom surface at approximately  $135^{\circ}$  as well. The final stage lasts for 35.6 milliseconds on average. The average remaining time for an opened keyhole is  $0.043\pm0.033$  s and  $0.029\pm0.043$  s for a closed keyhole. Fig. 3.22 also shows the shapes of the fusion zones in various stages. It can be seen that the bottom width in Fig. 3.22 (a) and (c) are narrower than the bottom width in Fig. 3.22 (b) and (d).

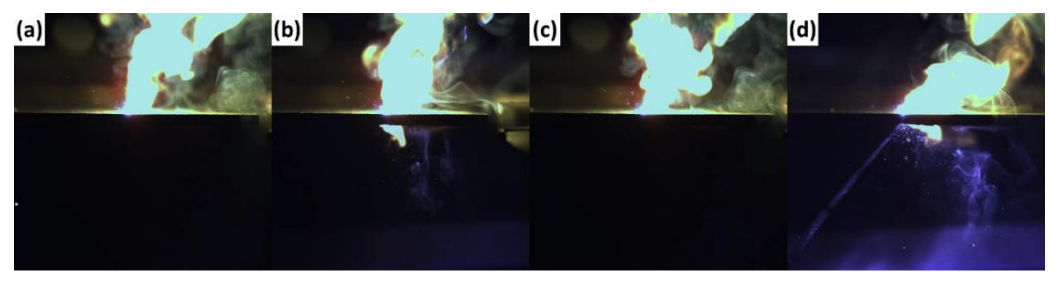


Fig. 3.21. Still images of the distinct stages of the plasma plume ejection in sequential order when  $\alpha$  is 135°. (a) The laser beam impinges on the top surface and the keyhole is closed, the plume ejects only from the top surface with an  $100^{\circ}$ - $105^{\circ}$  angle, (b) The keyhole opens in the bottom and a small part of plume ejects from the bottom with an angle close to  $90^{\circ}$ . This stage lasts for approximately 7.5 ms on average, (c) The keyhole bottom closes again, and the ejection angle of the plume is enlarged, (d) The keyhole bottom opens, and most of the plume ejects with an angle around  $135^{\circ}$ , a small portion of plume ejects from the bottom with an angle close to  $135^{\circ}$  as well. This stage lasts for 35.6 ms on average.

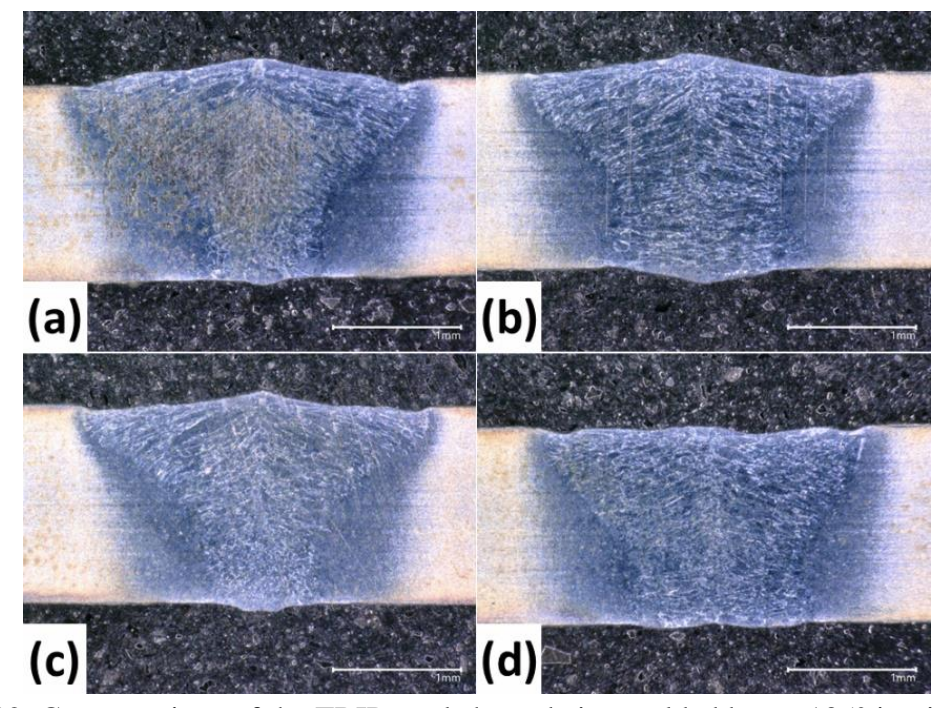


Fig. 3.22. Cross sections of the TRIP steel sheets being welded by an 135° impinged laser beam.

As shown in Fig. 3.23, the waist width, which is defined as the narrowest width of the keyhole cross section, becomes narrower when the incident angle increases from 90° to 120°, as it is concluded from Fig. 3.20 (d) (e) that, the amount of plasma plume ejected from the bottom is less than the perpendicular impinging case. Additionally, the standard deviation of the waist widths shows an increasing trend with the incident angle, revealing that the extent of erratic process behavior becomes more severe as the incident angle increases in a trailing configuration.

However, when the incident angle increased to 135°, where the keyhole transformed into an unstable state, the waist width of the keyhole fluctuated drastically. The minimum width is 0.397 mm, while the maximum width reaches 1.212 mm, which is wider than the keyhole waist generated by an incident angle of 90°.

The distance between the top surface of the metal sheet and the waist of the keyhole reflects the extent of heat transfer along the thickness. Fig. 3.23 (a) demonstrated that as the incident angle increases within a trailing configuration when the incident angles α are lower than 90°, the top surface-to-waist distance shows an increasing tendency. For the welding configuration with incident angles of 45° and 60°, full penetration was not generated along the weld. This phenomenon can be explained by considering that the laser beam impinges on the rear of the inclined weld pool is reflected to the environment without being absorbed, and the surface tension coefficient at the centerline is lower than the surface tension of the surrounding liquids. The thermal convection through the Marangoni flow delivers heat to the trailing end and the side boundaries of the bead. Additionally, the recoil pressure caused by the evaporation pushes the molten metallic to accumulate. Therefore, the heat is not effectively transported in the plate thickness direction. In comparison, the obtuse incident angles of 120° and 135°, can create full penetration during the welding process. The alternating partial and full penetration can be related to the laser-metal interaction (Liao & Yu, 2007). Since reflection and refraction are also involved in metal-laser interaction (Liao & Yu, 2007).

A laser beam in an obtuse incident angle impinges onto the keyhole wall and is reflected to the bottom of the keyhole. This preliminary opens the keyhole at the bottom surface. Additionally, more heat is supplied to the front wall of the keyhole (Khan, et al., 2022) and generates molten metal flow in front of the heat source (Kumar, Mukherjee, & Bandyopadhyay, 2017). This flow causes the cyclic collapse of the keyhole front wall and results in the cyclic opening and closing of the keyhole (Khan, et al., 2022). The interaction between the laser and the metal is also reflected in the angle of the plume ejection. The distorted and inclined plasma columns are shorter in length and bring exacerbated turbulence (Khan, et al., 2022). Due to the high cooling rate of steel sheets, the molten metal solidifies at a high rate (Khan, et al., 2022). Hence, as plotted in Fig. 3.23(b), a large deviation in the width of the bead occurred. In conclusion, an elliptical beam spot created by an inclined laser beam leads to an extended weld pool and comparing between the case when  $\alpha$  equals to  $45^{\circ}$  and  $60^{\circ}$ ,

the inclination of the plume enhances the extension as depicted in Fig. 3.23 (b), the impact on the weld pool length on the hot cracking susceptibility will be discussed in Chapter 3.6.

As shown in Fig. 3.23 (a), the beads created by tilted incident angles have larger widths than welding with a laser beam perpendicularly to the sheet. The width is positively correlated to the angle between the beam and the normal vector of the sample surface. The molten liquid driven by the Marangoni flow is transported to the surface along the keyhole and brings heat to the top surface and widens the top width of the bead (Kumar, Mukherjee, & Bandyopadhyay, 2017).

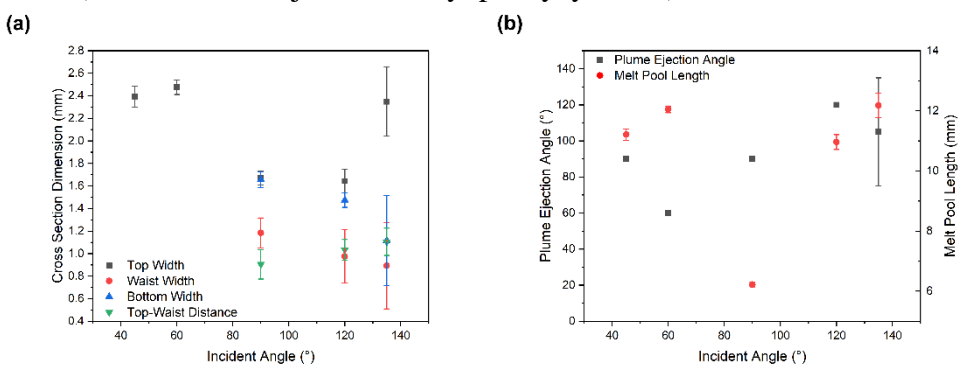


Fig. 3.23. (a) Geometrical parameters of the cross section of the bead, (b) Melt pool length and plume ejection angles correspond to various incident angles.

### 3.4 Fluid Flow Behaviour

In order to obtain in-situ observations for the behavior of the keyhole and the fluid flow during the welding process, a Cavitar® VCXG-15M welding camera is applied to capture the welding process at a frame rate of 100 FPS. The experimental setup used is described in chapter 2. The welding conditions studied include the variation in incident angle of 90° and 45°. Before each experiment, a ruler is placed on the welding path to serve as a scale bar for measuring the dimensions of the weld pool and the bead.

#### 3.4.1 Kevhole Mode

Fig. 3.24 is a welding process using a laser beam with a 0.6 mm diameter and an incident angle of 90°, a travel speed of 40 mm/s at 5 mm from the free edge, to generate an open keyhole and a solidification crack.

As marked on Fig. 3.24, the bright part in the bead represents the molten liquid, where the melt pool shows an elliptical shape, and followed by the mushy zone where liquid and solid coexist. The dark part represents the resolidified solid, because of diffuse reflection on the rough surface created by rapid cooling of the heated turbulent flow. The still frames in Fig. 3.24 show that, at t<sub>0</sub>+0 ms, the heated molten fluid flow surges up, and suppresses at t<sub>0</sub>+10 ms. It is measured that

the crack starts to initiate at 7.4 mm behind the end of the melt pool. Additionally, it could be inferred that the velocity of the solidification front, denoted by R, is constant if the travel speed of the beam spot remains constant.

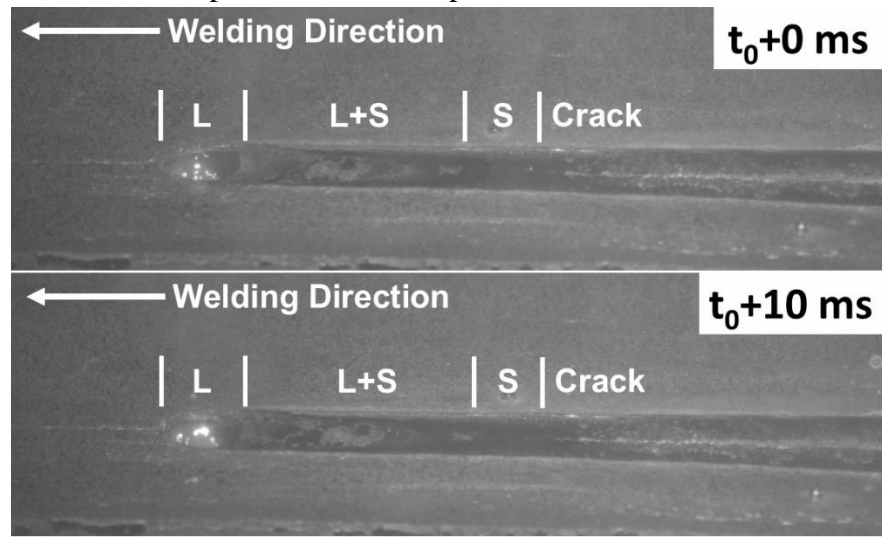


Fig. 3.24. Behavior of the welding seam and the crack during a welding process with a power of 4000 W, a beam size of 0.6 mm, an incident angle of  $90^{\circ}$ , a travel speed of v=40 mm/s, at 5 mm from the free edge.

When the crack develops through the steel plate sample, the part between the free edge and the bead falls off and shows the development of the melt pool along the longitudinal cross section. But due to the high solidification rate, the liquid resolidifies rapidly and forms bridging between the rest of the steep plate and the fallen part. The teardrop shape cavity on the edge reveals the distribution of the liquid, since the heat is dissipated in the top and bottom surface through convection, and in the transverse direction through conduction as well.

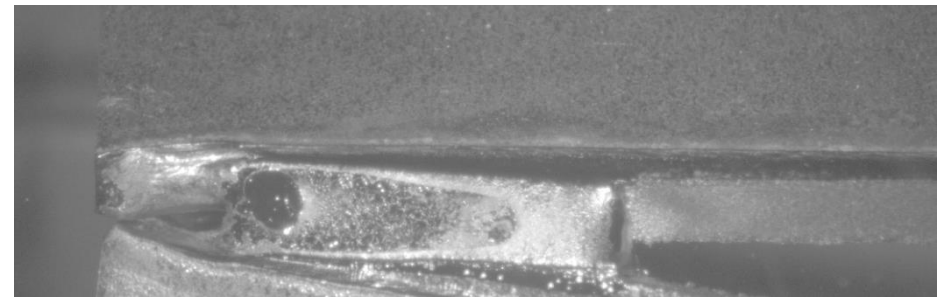


Fig. 3.25. Still frame of the moment when the part cut by the crack falls off during a welding process when P=4000 W, d=0.6 mm,  $\alpha$ =90°, v=40 mm/s, at 5 mm from the free edge.

### 3.4.2 Conduction Mode

Fig. 3.26 shows the welding process operated in conduction mode when  $\alpha$  is set as 45°. With a leading configuration where the incident angle is acute, the melt pool forms an elliptical shape, and the rear part of the wall fluctuates more

severely since more heat is delivered to the rear boundary. As shown in Fig. 3.26, at  $t_0+0$  ms, the fluid in the rear part is suppressed, and at  $t_0+20$  ms, the fluid surges up by the heated fluid flowing from the bottom to the top.

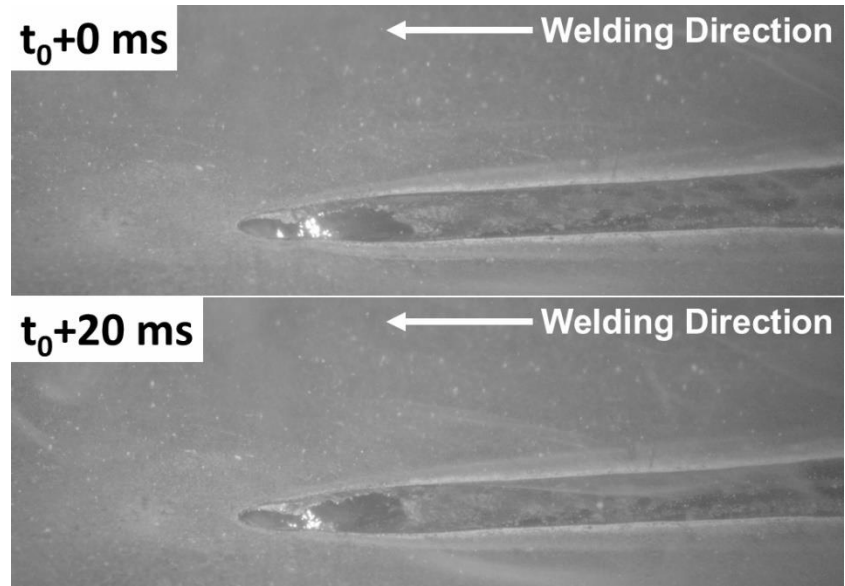


Fig. 3.26. Behavior of the welding pool and the seam during a welding process with v=40 mm/s, P=4000 W, d=0.6 mm,  $\alpha$ =45° and at 10 mm from the edge.

## 3.5 Transient Temperature

The performance related to the absorptivity of laser energy, and the thermal gradient during the welding process can be reflected by the temperature field developed around the welding site. To observe the thermal behavior of the TRIP steels sheets under different welding conditions, three thermocouples, with a diameter of 0.25 mm are attached to measure the transient temperature during welding process. As shown in Fig. 3.27, three conditions are selected: (a):  $\alpha = 90^{\circ}$ , d=0.6 mm, (b):  $\alpha=135^{\circ}$ , d=0.6 mm, (c)  $\alpha=90^{\circ}$ , d=0.2 mm. All three welding conditions are operated in penetration keyhole mode, the temperature in the centerline exceeds the melting temperature. At a distance of 1 mm away from the centerline, the peak temperature and maximum cooling rate recorded during the in-situ measurement are listed in Table 3.4. According to the heat conduction equation, the heat flow rate is proportional to the temperature difference between a high temperature region and low temperature region (Hahn & Özisik, 2012). Hence, the highest peak temperature is observed during the case when d=0.6 mm and  $\alpha=135^{\circ}$ , indicating the highest thermal gradient. The maximum cooling rate is recorded at 0.108 s after the temperature reached the peak in the case for d=0.6 mm and  $\alpha=135^{\circ}$ , which is 2400 °C/s. A minimum cooling rate of 1300 °C/s is recorded at 0.142s after reaching the peak temperature in the case when d=0.2 mm and  $\alpha$ =90°. Such a difference between thermal behavior can be explained by the fact that a laser beam impinged at an incident angle of  $135^{\circ}$  can be reflected on the front wall of the keyhole and induce more reflection inside the keyhole (Liao & Yu, 2007). Additionally, the inclined beam provides a larger interaction area with the material, which enhances the absorption. In comparison, the welding condition with d=0.6 mm and  $\alpha$ =90° induces less reflection because of the orthogonal impingement, and there is also less interaction area between the beam and the material. Compared to the case when d=0.6 mm, a spot diameter of 0.2 mm generates the lowest temperatures and cooling rates, due to the high energy density in the weld pool center that let the laser beam penetrate through the steel sheet, which is not absorbed by the material and transformed into thermal energy.

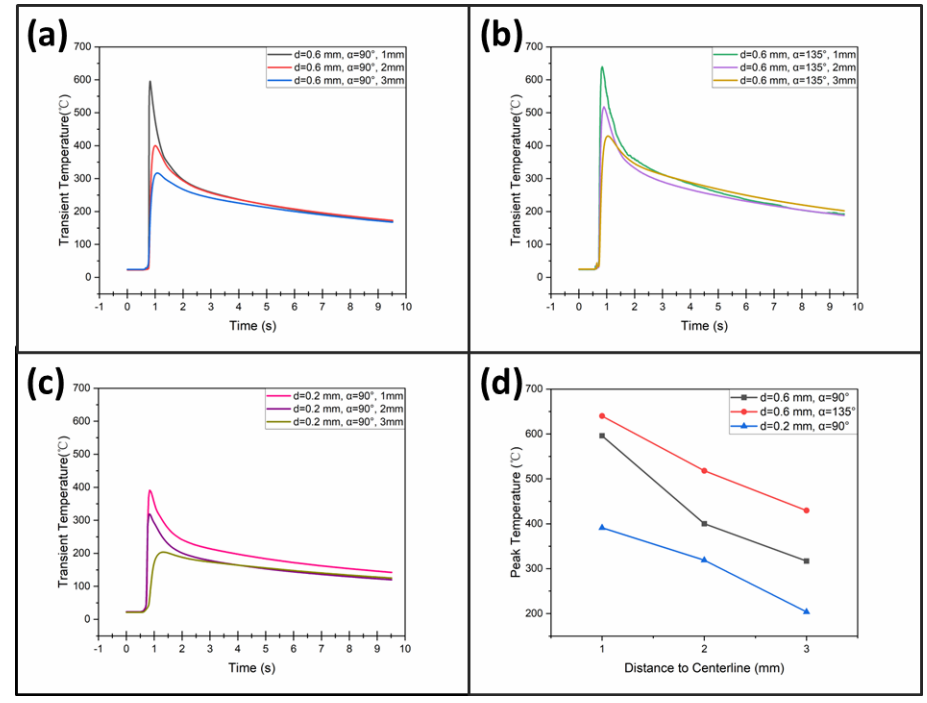


Fig. 3.27. Temperatures recorded at 1mm, 2mm, 3mm from the centerline as a function of time, at (a)  $\alpha$ =90° d=0.6 mm, (b) $\alpha$ =135°, d=0.6 mm, (c)  $\alpha$ =90°, d=0.2 mm. (d) Peak temperature as a function of distance from the centerline during a welding process with different welding conditions.

Table 3.4. Peak temperature and maximum cooling rate recorded at 1 mm from the centerline during in-situ welding tests at different welding conditions.

Welding Condition	Peak Temperature (°C)	Maximum Cooling Rate (°C/s)
d=0.6 mm, α=90°	596.0	2400
d=0.6 mm, α=135°	639.9	4900
d=0.2 mm, α=90°	391.3	1300

## 3.6 Hot Cracking Susceptibility

Free-edge welding tests are conducted to quantify the hot cracking susceptibility among different welding conditions. The conditions that obtain full-length crack at the farthest distance from the free edge correspond to the highest cracking susceptibility. The measured crack lengths are shown in Fig. 3.28, except for the two cases when  $\alpha$ =45°, d=0.6 mm and  $\alpha$ =90°, d=1.2 mm, which are not able to fully penetrate the sheet. The reason why the welding condition when  $\alpha$ =60° and d=0.6 mm is able to generate cracks can be explained by the heat accumulates in the region closed to the edge and can only dissipate by convection. This phenomenon deviates the dimension of the melt pool, and the accumulation enhances penetration.

Welding with d=0.2 mm and  $\alpha$ =90° shows the lowest susceptibility, and the condition when  $\alpha$ =135°, d=0.6 mm has the second lowest susceptibility. Both 120° and 60° incident angles result in a full crack at a distance of 5 mm from the edge. For the condition of  $\alpha$ =90°, d=0.6 mm a full crack length is even observed for a distance of 6 mm from the free edge and corresponds to the highest cracking susceptibility. It can be concluded in Fig. 3.12 and Fig. 3.23 that a spot of smaller diameter creates a narrower bead, the solidification shrinkage is less and induces less strain, and an inclined beam that prolongs the heated area, and acts as pre-heating or post-heating processes. This effect ensures the liquid has sufficient time to heal the cracks.

It is worth noting that the reason the average crack in some distances nearer than 5 mm does not reach 45 mm is because of the recovery of the resolidified material in the entrance of the sheet. Additionally, at the end of the welding process, when the welding spot moves to the boundary of the steel sheet, the part between the bead and the free edge does not completely fall off due to the bridging effect as Fig. 3.25 depicted.

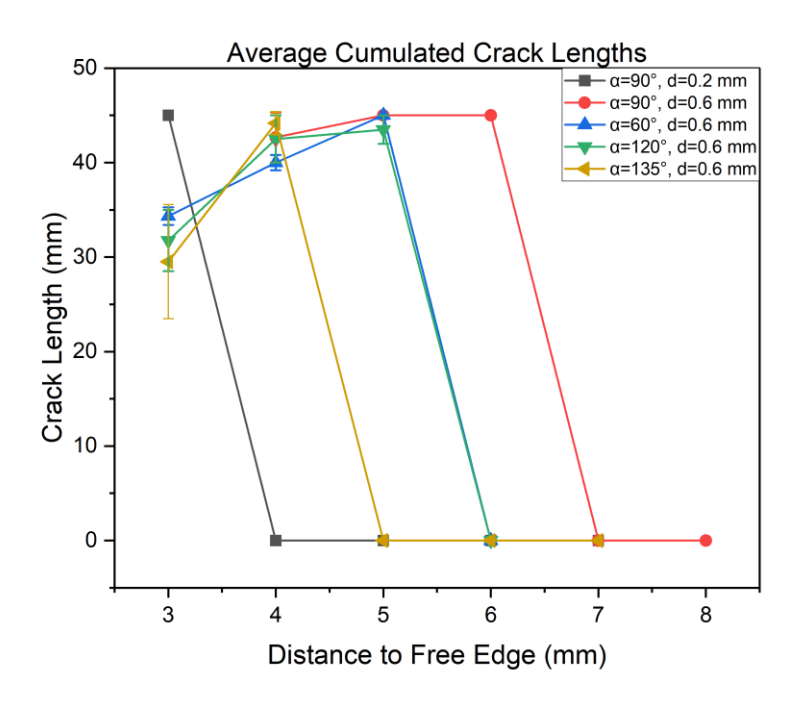


Fig. 3.28. Length of the cracks generated by welding processes with various incident angles and spot diameters as functions of the distance to the free edge, under a 4 kW Nd: YAG laser with 1030 nm wavelength, and a travel speed of 40 mm/s

## 3.7 Microstructure

Fig. 3.29 shows the microstructure obtained by SEM from a top view perspective with a welding direction from right to left. In fig 1a a macrograph shows the weld bead and the crack form. The grains in the HAZ grow in an equiaxed shape. At the fusion zone, the grains grow into columnar geometries. Fig. 3.29 (b), obtained with a magnification of  $1000\times$ , shows that the solidified material grows into columnar grains . In the region in front of the crack, the columnar grains bend towards the trailing end of the melt pool corresponding to the largest thermal gradient, but in the crack region, the epitaxially grown grains do not bend, and the growth direction is orthogonal to the crack.

The density of solid metal is higher than the molten metal, the material within the mushy zone undergoes shrinkage during solidification and creates liquid channels between the columnar grains, hot cracking is initiated if the liquid feeding rate cannot compensate the shrinkage rate (Zhao, Wu, Zhang, Kong, & Liu, 2022)

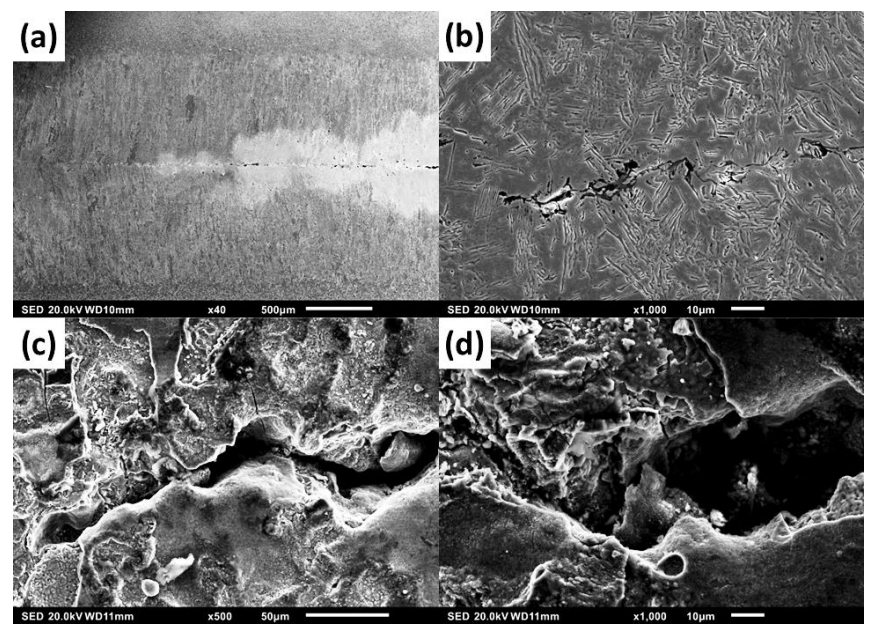


Fig. 3.29. SEM image with original magnification of (a)  $\times 40$ , (b)  $\times 1000$ , (c)  $\times 500$  unprepared sample, (d)  $\times 1000$  unprepared sample. Solidification crack generated by a laser beam with a 90° incident angle, a spot diameter of 0.6 mm and a travel speed of 40 mm/s at 5 mm from the free edge.

Because of the high cooling rate and short cooling period, the solidification time is too short for the solution to redistribute (Lippold, 2015). The melt convection in the melt pool is not vigorous enough to form a homogeneous composition of the melt (Kou, 2003). The metallurgical effect of segregation of different compositing elements is considered for their various melting points. Fig. 3.30 and Table 3.5 showed the elemental composition of Fe, Al, Si and Mn in the base material, the boundary of the fusion line, the fusion zone, and the centreline of welding, where the liquid film experiences a tensile force during crack propagation. The difference between the amount of Fe and Al in the base material and the centreline is approximately 0.4% and 1.4%, respectively. More Si is presented at the fusion zone boundary and the centreline, on the contrast, compared to the composition in the base material, Mn is less distributed in the fusion zone. It is inferred that Si is contained in high melting point phases, while Mn is burned off by the high temperature during laser welding.

Table 3.5. Semi-quantitative SEM-EDS elemental analysis of different regions.

Element	Base Material	se Material Boundary Fr		Centerline
	(wt%)	(wt%)	(wt%)	(wt%)
Fe	96.905±0.13	97.26±0.13	97.28±0.13	97.16±0.12
Al	0.690±0.02	0.68±0.02	0.63±0.02	0.70±0.02
Si	0.265±0.02	0.33±0.02	0.28±0.02	0.37±0.02
Mn	2.135±0.04	1.73±0.04	1.81±0.04	1.78±0.03

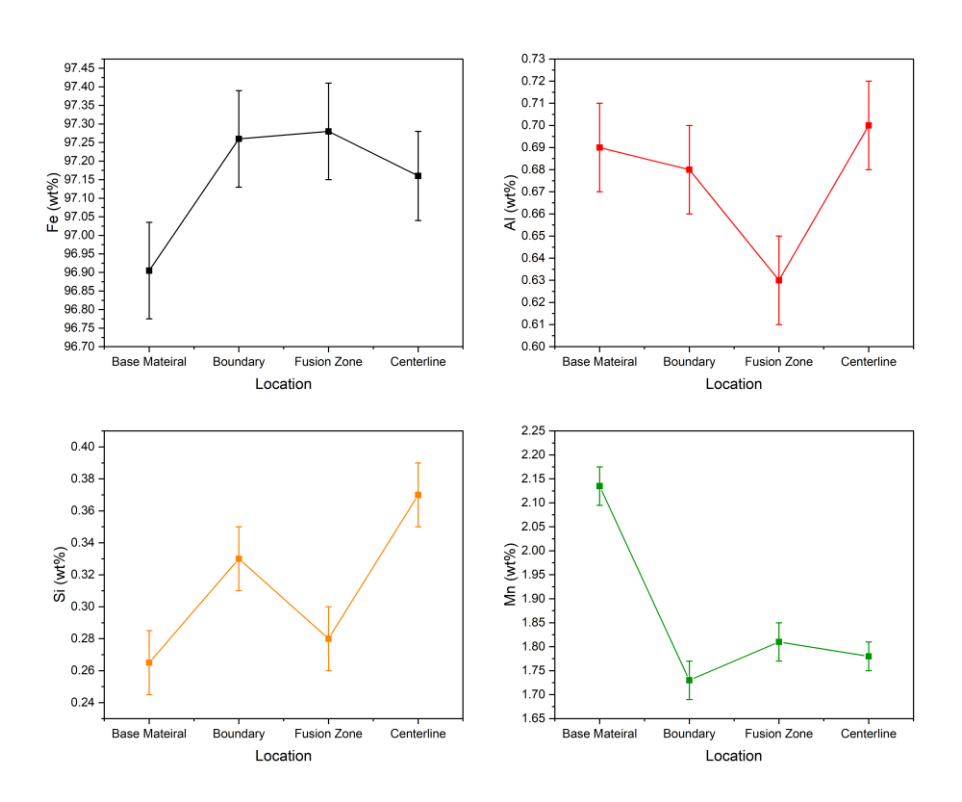


Fig. 3.30. Semi-quantitative SEM-EDS elemental analysis of different regions.

Fig. 3.31 and Fig. 3.32 show the grain growth orientations for different beam sizes and incident angles. The columnar grain widths, calculated by line intersection method from Fig. 3.11, Fig. 3.5, and Fig. 3.20, are listed in Table 3.6 and 3.7, and depicted in Fig 3.33. The refinement of grains, and thus more grain boundaries, reduce the strain partitioned per grain boundary (Böllinghaus & Herold, 2005), and mitigates the hot cracking susceptibility by preventing the liquid film from rupturing (Pellini, 1952).

As mentioned in Chapter 1, the product of temperature gradient G and the solidification rate R determines the size of the grains (Schempp, et al., 2014) (Lei, et al., 2023) and higher  $G \times R$  refers to higher solidification rate (Lei, et al., 2023). It is also observed in Chapter 3.4.1 that the speed of growth of the solidification front remains constant if the travel speed of the laser spot remains constant. Among the cases of various spot sizes and incident angles, the travel speed is maintained at 40 mm/s, the solidification rate R at the center line of the bead can be considered constant among all situations. As the incident angle  $\alpha$  maintains at 90°, the difference in the average grain width welded by beams with spot diameter 0.6 and 0.2 mm is less than the standard deviation. For the spot size of 1.2 mm a grain width reduction is observed. As mentioned in Chapter 3.5, the welding condition when  $\alpha$ =135° and d=0.6 mm corresponds to the highest cooling rate and the highest peak temperature, which gives

the highest G×R value. Hence, as shown in Fig. 3.33 (b), in the trailing configuration when  $\alpha$ >90°, the average width of columnar grains decreases as the incident angle increases.

It can be also seen from Fig. 3.33 (a) and (b) that the average width of the grains welded in conduction and transition keyhole mode are lower than those welded by penetration keyhole mode. It can be explained that the weld pool does not fully penetrate the steel plate, the weld pool is surrounded by solid materials with a larger heat conduction constant, that promotes the dissipation of heat. Additionally, at the leading configuration with incident angles  $\alpha$  smaller than 90°, the thermal heat is delivered to heat and vaporize the rear part of the welding pool and induce perturbation during solidification and refines the grains

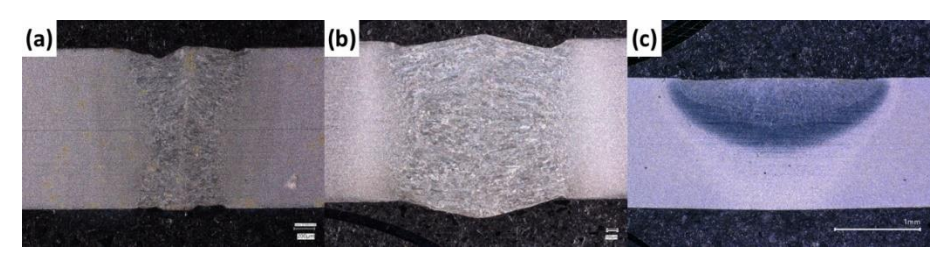


Fig. 3.31. Optical microscopic top view of the fusion zone welded by laser beams with a spot diameter of (a) 0.2 mm, (b) 0.6 mm, (c) 1.2 mm, a power of 4000 W, an incident angle of  $90^{\circ}$  and a travel speed of 40 mm/s.

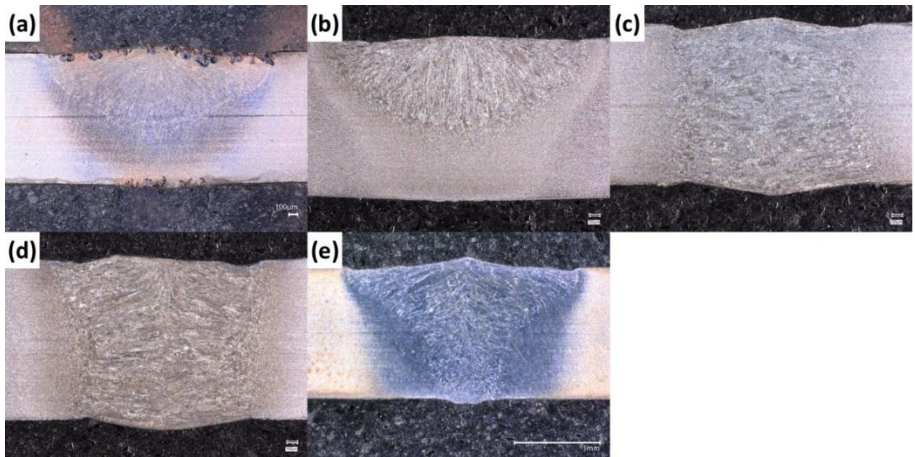


Fig. 3.32. Optical microscopic top view of the fusion zone welded by laser beams with an incident angle of (a)  $45^{\circ}$ , (b)  $60^{\circ}$ , (c)  $90^{\circ}$ , (d)  $120^{\circ}$ , (e)  $135^{\circ}$ , a power of 4000 W, a beam spot diameter of 0.6 mm and a travel speed of 40 mm/s.

Table 3.6. Width of columnar grains among the samples welded by laser beams with a power of 4000 W, an incident angle of 90°, a travel speed of 40 mm/s and various spot diameters.

Spot Diameter (mm)	0.2	0.6	1.2
Grain width (μm)	38.97±8.23	41.19±9.24	19.28±4.66

Table 3.7. The width of columnar grains among the samples welded by laser beams with a power of 4000 W, a beam spot diameter of 0.6 mm, a travel speed of 40 mm/s and various incident angles.

Incident Angle (°)	45	60	90	120	135
Grain width (µm)	25.65±7.61	28.23±8.45	41.19±9.24	36.66±7.91	35.31±7.69

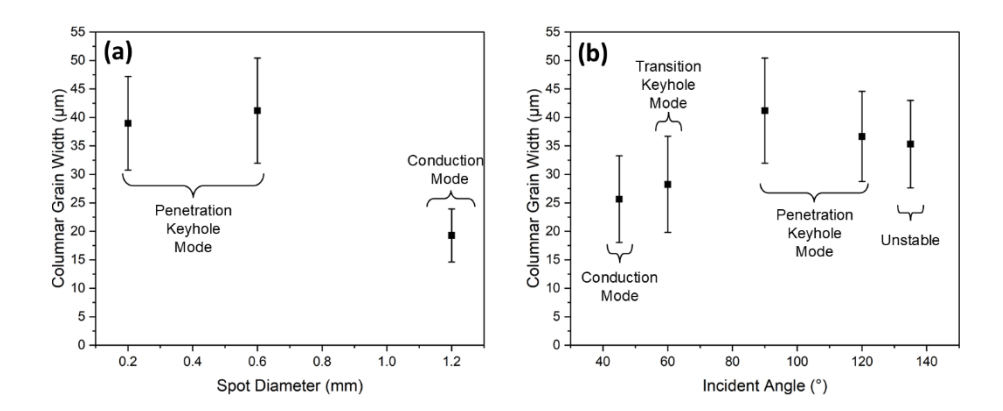


Fig. 3.33. The width of columnar grains among the samples welded by laser beams with a power of 4000 W, a travel speed of 40 mm/s and (a) various spot diameters when the incident angle is  $90^{\circ}$ , (b) various incident angles when the beam spot diameter is 0.6 mm

## 4 Disscussion

During the formation of cracks, the presence of a semisolid state is a prerequisite (Eskin & Katgerman, 2007). The difference between the density of liquid and solid results in solidification shrinkage followed by the nonuniform thermal contraction of the cooling material. When the coalescence temperature is reached in the final stage of solidification, tension stress is exerted when solidification shrinkage takes place (Eskin & Katgerman, 2007). Due to the high post-welding cooling rate (Chande & Mazumder, 1984) there is less abundant time for the back filling liquid to heal the gaps between the solidified columnar grains (Eskin & Katgerman, 2007). According to Prokhorov and Rappaz et al.'s theory, hot cracks are initiated if the maximum mesoscopic strain rate of solidification shrinkage exceeds the maximum value that the semisolid can endure (Prokhorov, 1956) (Rappaz, Drezet, & Gremaud, A new hot-tearing criterion, 1999).

As mentioned in Chapter 1, hot cracking is the result of a complex interaction of factors, including metallurgical and mechanical effects. The laser process parameters will result in the formation of a melt pool. When the power density increases, the distribution of heat in the material to be welded will shift from a conduction mode to a keyhole mode. This transition is related to the recoil pressure from vaporizing metal creating in first instance a shallow hole, which is extended when multiple reflections inside the hole will occur, as depicted schematically in Fig. 1.2 in Chapter 1.

The absorption of laser energy is strongly enhanced within the keyhole, promoting full penetration of the sheet. In that respect, laser power and laser spot size play an important role in ensuring boiling of the material. If an open keyhole is realized, energy will be lost, and a plume will be generated at the back side of the plate. However, when the plume ejects from the top surface laser energy will be absorbed reducing the efficiency of the process.

Another primary process parameter is the travel speed of the heat source with respect to the base plate. Increasing travel speed will reduce the amount of heat per unit length of weld and therefore affect the dimensions of the melt pool.

The processing parameters and the resulting melt pool shape will dictate the evolution of the microstructure. Cooling rate and the direction of the maximum temperature gradient determine the grain size and texture. The restraints exposed on the solidifying melt pool eventually create cracks.

In order to realize an appropriate weld bead in the 1.5 mm thick steel sheet. Preliminary experiments were conducted to establish the welding condition that form fully penetrated welds. These experiments were all conducted at a laser power of 4 kW, a spot diameter of 0.6 mm and an incident angle of 90°, while the travel speed was varied. With an increase in travel speed the heat input is reduced and the weld pool width decreased as shown in Fig. 3.4. For the remainder of the welding experiments, a travel speed of 40 mm/s was selected.

In this study the effect of the laser beam characteristics on the sensitivity of the material to hot cracking is investigated. The power density can be adjusted by changing the power or focal spot size and by the tilting angle of the beam. In the study described in this thesis the power is maintained at 4 kW. The spot size varied from 0.2 to 1.2 mm. The tilting angle of the incident beam was changed from a trailing to a leading configuration (45° to 135°), with a perpendicular beam (90°) being the reference value.

In the study of the effect of laser spot size with a  $90^{\circ}$  incident angle, when the object distance increases from the focal distance, where the laser spot diameter d is 0.2 mm, to the distance where d=1.2 mm, the power delivered to the surface is dispersed, resulting in a decreasing power density, which is in reverse proportion to the square of the spot radius. The power density corresponding to a spot diameter d=0.2 mm is 9.13 times the power density where d=0.6 mm, and 36.48 times the power density where d=1.2 mm.

As shown in the still images in Fig. 3.11 (a)-(c) and the cross sections in Fig. 3.11 (d)-(f), a very concentrated laser beam (d=0.2 mm) leads to the formation of an open keyhole. This results in a relatively low energy absorption rate as much of the laser energy passes through the opened keyhole without being absorbed for melting metal. Pan performed calorimetric measurements during laser welding of zinc coated steels and estimated the energy loss through the keyhole to be around 40% (Pan, 2011). At the same time the plume is mostly created at the back side of the workpiece, which prevents the absorption of beam energy for enlarging the melt pool. The resulting cross section width of the bead is relatively small. As the area of the beam spot increases, the absorption rate of laser power increases. The catenoid shaped full penetration keyhole is wider. The created plume in this configuration is also escaping from the top surface, which might result in the absorption of a certain amount of energy. Pan estimated this energy loss combined with losses by reflection, radiation and convection to be around 8% (Pan, 2011). The direction of the generated plume is related to the geometrical shape of the keyhole. If the incident angle of the beam is 90°, the keyhole can be expected to be perpendicular to the plate surface, as is the plume angle. This can be seen from the images depicted in Fig. 3.5, Fig. 3.6 and Fig. 3.11.

The increase in energy absorption in the plate is supported by the temperature measurements displayed in Fig. 3.27 (a) and (c). The peak temperatures at certain distances from the fusion lines are significantly lower for the 0.2 mm spot diameter, indicating the energy loss by the open keyhole.

For both keyhole conditions the columnar grains grow perpendicular to the fusion zone. A distinct centerline can be observed where the grains from both sides of the weld pool meet, in particular for the smallest beam diameter. Liquid metal will be present at this location in the final stage of solidification, which might make it prone to hot cracking.

When the power continues to disperse as the spot diameter further increases, the power distributed onto a unit area reduces. Not enough heat is delivered to evaporate a significant amount of metal, and the welding mode is then transformed from keyhole mode to conduction mode. The plume created will only escape from the top surface, lowering the

absorption even further. The direction of grain growth is still perpendicular to the fusion line, but due to the shape of the melt pool, the grains at the center line have a different appearance by growing towards the surface centerline. In addition, the solid metal adjacent to the weld pool enhances heat dissipation, which increases the cooling rate and reduces the grain size. This is to be expected as indicated in Fig. 1.4, in Chapter 1, when  $G \times R$  increases the size of the solidification structure decreases. As full penetration is not achieved under these conditions, an appropriate weld cannot be realized. This condition should therefore not be regarded with respect for hot cracking sensitivity.

The width of the columnar grains in the fusion zones reflects the conditions of solidification. As shown in Fig. 3.33 (b), when the incident angle remains at  $90^{\circ}$ , the average columnar grain width for a beam with a 0.2 mm spot diameter and a 0.6 mm spot diameter is approximately similar to around 40  $\mu$ m, within the range of standard deviation. When strain partitioning is considered, the conditions of the 0.2 mm beam spot would result in a smaller bead width, associated with less solidification shrinkage.

It should also be mentioned that the experiments described above are at a distance of 13 mm from the free edge, where no cracks occurred at this location. In the free edge hot cracking tests, the distance from the free edge is reduced, which causes heat accumulation at the free edge side that aids the deepening of the fusion zone. In combination with the stresses introduced, cracks may result.

Considering the effect of the laser spot diameter, the hot cracking test results showed in Fig. 3.28. revealed that the hot cracks for a 0.2 mm spot size are not observed anymore at a distance of 4 mm from the free edge. For the 0.6 mm spot the distance from the free edge to realize crack free welds should be increased to 7 mm. If the spot size is further increased to 1.2 mm, the weld is only partially penetrated, and this condition should be omitted. To achieve full penetration in this case, the laser power should be increased or the travel speed decreased. This would however lead to a very wide weld pool width, which will promote hot cracking.

In the study of the effect of different incident angles with a fixed beam spot size, the variation of the incident angle in the longitudinal direction transforms the circular spot to an elliptical spot. By tilting the laser beam, the spot width remains approximately 0.6 mm, whereas the length of the spot in the longitudinal direction is extended. As indicated in Table 3.3, the spot area increased when tilting the beam. The incident angle is defined as the angle between the beam and the original surface of the bead. It should however be kept in mind that when the melt pool is formed, the surface will deform, altering the incident angle with respect to the newly formed surface orientation. This will be the case when keyholes are formed. It is good to mention that over a large range of incident angles the difference in absorption rate can be neglected, as was indicated in Fig. 1.1 in Chapter 1.

During a welding process, the prolonged impingement area acts as a pre-heating process in case of an obtuse incident angle, where the beam is directed towards front wall of the melt pool. For acute incident angles, the beam impinges on the molten liquid and acts as a post-heating process, as was schematically presented in Fig. 3.13. Thus, by tilting the laser beam the energy density distribution is affected and the location of the highest energy density is shifted.

If the acute incident angle is too low, i.e. 45°, full penetration is not achieved, as shown in Fig. 3.32 (a) and (b). For these conditions, similar arguments compared to the perpendicular beam with a spot size of 1.2 mm is valid. The energy density is not enough to result in sufficient evaporation to initiate a keyhole by the recoil forces. The generated laser plume only escapes from the top surface perpendicularly, instead of in the impingement direction of the laser beam. The heat introduced in the plate is not efficiently transported to the back surface of the plate but broadens the weld pool as indicated in Fig. 3.23 (a). The solid metal surrounding the melt pool effectively dissipates the heat introduced, also resulting in a relatively small width of the columnar microstructure as indicated in Fig. 3.33 and Table 3.7. With respect to hot cracking, these conditions should be neglected.

For the condition with an incident beam angle of 90° and 120°, full penetration is achieved with approximately symmetrical catenoid keyhole shapes, whereas for the case of 135° a tapered bead shape was found. For the former cases the grains grow parallelly to the plate surface towards the centerline. For the latter case a distinction should be made between the top and the root region of the bead. In the top region the grain orientation is perpendicular to the inclined fusion line, towards the top surface. In the root region the grains grow parallel to the plate surface. In addition, it should be emphasized that at an 135° incident angle, the process is not entirely stable resulting in variations in the bead shape and dimensions as displayed in Fig. 3.22. With respect to the direction of the plume it should be mentioned that the plume is escaping from the keyhole which direction shifts with the orientation of the laser beam. The plume direction is presented in Fig. 3.23 (b). In this figure it can also be seen that in the case of an unstable keyhole, which is the case of a tilting angle of 135°, the plume direction is varying significantly.

For the 90° and 120° incident angles, the bead width is approximately the same, which would result in a similar solidification and thermal contraction. However, the cracking susceptibility is somewhat reduced for 120°. A crack free bead is obtained even at 6 mm from the free edge, compared to 7 mm for the perpendicular beam. It can be hypothesized from Fig. 3.23 (b) that the prolonged melt pool length indicating a longer heated region can be the reason for this reduction, for ensuring longer time for the back filling liquid to heal the cracks, while a opened keyhole brings the heat through fluid flow towards the melt pool bottom instead of broadening the bead width. It was found that the columnar grain width is slightly reduced at 120°. Another aspect is the fluid flow in the melt pool which may affect the liquid feeding towards the mushy zone.

In the case of a trailing configuration where  $\alpha > 90^{\circ}$ , more energy is delivered to the solid front wall of the keyhole, melting the metal in front of the heat source and generating fluid flows. The solid front wall also reflects the beam inside the weld pool that promotes the absorption of laser energy and aids the opening of the keyhole root, therefore, the peak

temperature in the case of an 135° incident angle is higher than the temperature in the case of a 90° incident angle, as shown in Fig. 3.27 (a) and (b). It is reported that a turbulent flow may cause the keyhole front wall to collapse periodically (Khan, et al., 2022) (Kumar, Mukherjee, & Bandyopadhyay, 2017).

This could be the case for the instability of the incident angle of 135°. The topic of keyhole stability and dynamics is complex and would require detailed studies that are beyond the scope of this thesis. Such a study should include aspects of fluid flow in the melt pool, as this could promote liquid feeding towards the hot cracking sensitive location. The results of this investigation reveal that the stability of the keyhole and thus the process can be estimated by the plume behavior. An erratically moving plume indicates the process stability is not optimal and variations in bead dimensions can be expected.

Apart from the effects described above, also the metallurgical effect of segregation should be considered. The global measurements of the composition are not conclusive in this respect. Detailed information on the composition at the grain boundaries is required to estimate the effect of laser parameters on the presence of low melting point phases that will influence the cracking susceptibility. In this study only one material composition is considered. The segregation effects in case full penetration of the weld pool in the plate is achieved will be not significantly different for the welding conditions prevailing.

In conclusion, the study of selecting process conditions with respect to beam shape and energy density distribution, i.e. laser beam shaping, to minimize the hot cracking sensitivity for laser welding in TRIP steel sheets, shows that a slightly tilted incident angle of the laser beam to a leading configuration ( $\alpha$ <90°) is preferred. The incident angle should not be too low, otherwise full penetration will not be achieved. Furthermore, a smaller spot size appears to result in a lower hot cracking tendency. Although energy is lost via the open keyhole, the reduced heat input in the plate results in a narrower weld pool accompanied by a smaller solidification shrinkage.

## 5 Conclusion

The study of beam shaping focuses on the modification of the beam size and the incident angle of the beams. Based on the results, the following conclusions can be drawn:

- 1. The modification of beam size changes the density of power delivered to the surface. A concentrated beam generates a narrow bead, which mitigates the hot cracking susceptibility by reducing thermal contraction and external tension. A smaller spot size results in a lower energy absorption rate, i.e. larger energy waste. Hence, it is recommended to adjust the power at certain thickness to save energy loss while maintaining the size of the melt pool to not be too large so that it is easier to crack.
- 2. A tilted incident beam forms an elliptical spot and extends the solidification time, which is beneficial for mitigating the hot cracking susceptibility though enhancing the back flow of liquid and healing cracks.
- 3. In the case of a leading configuration of the laser beam, the penetration depth is decreased, leading to partial penetration, which is not acceptable for welds, But more heat is delivered to the mushy zone and suppresses the hot cracking susceptibility. Therefore, a proper acute angle should be carefully selected to ensure full penetration.
- 4. In a trailing configuration of a laser beam, a tilted incident angle of 135° will lead to the risk of generating erratic fluid flow and producing an unstable keyhole. This affects the weld quality and should be avoided in industrial production.

# **Bibliography**

- Agarwal, G. (2019). Study of Solidification Cracking during Laser Welding in Advanced High Strength Steels. A Combined Experimental and Numerical Approach. Delft: Delft University of Technology.
- Ai, Y., Jiang, P., Wang, C., Mi, G., Geng, S., Liu, W., & Han, C. (2018, August). Investigation of the humping formation in the high power and high speed laser welding. *Optics and Lasers in Engineering*, 107, 102-111. doi:10.1016/j.optlaseng.2018.03.010
- Alvarez, P., Vázquez, L., Ruiz, N., Rodriguez, P., Magaña, A., Niklas, A., & Santos, F. (2019). Comparison of Hot Cracking Susceptibility of TIG and Laser Beam Welded Alloy 718 by Varestraint Testing. *Metals*, 9(9), 985. doi:10.3390/met9090985
- Baik, S., Kim, S., Jin, Y., & Kwon, O. (2001). Effects of Alloying Elements on Mechanical Properties and Phase Transformation of Cold Rolled TRIP Steel Sheets. *ISIJ International*, 41(3), 290-297. doi:10.2355/isijinternational.41.290
- Ban, H., & Shi, G. (2018). A Review of Research on High-Strength Steel Structures. *Structures and Buildings*, 171(8), 625-641. doi:10.1680/jstbu.16.00197
- Belhadj, A., Bessrour, J., Masse, J., Bouhafs, M., & Barrallier, L. (2010). Finite element simulation of magnesium alloys laser beam welding. *Journal of Materials Processing Technology*, 210(9), 1131-1137.
- Bertrand, C., & Poulon-Quintin, A. (2015). Temporal pulse shaping: a key parameter for the laser welding of dental alloys. *Laser in Medical Science*, *30*, 1457-1464.
- Böllinghaus, T., & Herold, H. (2005). *Hot Cracking Phenomena in Welds*. Berlin: Springer.
- Chande, T., & Mazumder, J. (1984, October 1). Estimating effects of processing conditions and variable properties upon pool shape, cooling rates, and absorption coefficient in laser welding. *Journal of Applied Physics*, 56, 1981–1986. doi:10.1063/1.334231
- ChenW., AckersonP., & MolianP. (2009). CO2 laser welding of galvanized steel sheets using vent holes. Materials & Design, 30(2), 245-251.
- Chihoski, R. A. (1972). The character of stress fields around a weld arc moving on aluminum sheet. *Welding Journal*, 51(1), 9.
- Coniglio, N., & Cross, C. (2016). Towards Establishment of Weldability Testing Standards for Solidification Cracking. In T. Böllinghaus, J. C. Lippold, & C. E. Cross, *Cracking Phenomena in Welds IV* (pp. 37-66). Berlin: Springer. Retrieved Feburary 11, 2016
- Coniglio, N., & Cross, C. (2020, April 29). Effect of weld travel speed on solidification cracking behavior. Part 1: weld metal characteristics. *The International Journal of Advanced Manufacturing Technology*, 107, 5011-5023.
- Cross, C. (2005). On the Origin of Weld Solidification Cracking. In T. Böllinghaus, & H. Herold, *Hot Cracking Phenomena in Welds* (pp. 3–18). Berlin: Springer.
- Dausinger, F., & Shen, J. (1993). Energy Coupling Efficiency in Laser Surface Treatment. *ISIJ International*, *33*(9), 925-933. doi:10.2355/isijinternational.33.925

- De, A. K., Speer, J. G., & Matlock, D. K. (2003, Feburary). Color tint-etching for multiphase steels. *dvanced Materials & Processes*, 161(2), 27-31.
- Eskin, D. G., & Katgerman, L. (2007, May 22). A Quest for a New Hot Tearing Criterion. *Metallurgical and Materials Transactions*, 38, 1511–1519. doi:10.1007/s11661-007-9169-7
- FaridM., & MolianP.A. (2000). High-brightness laser welding of thin-sheet 316 stainless steel. Journal of materials science, 35, 3817-3826.
- Feurer, U. (1977). Influence of alloy composition and solidification conditions on dendrite arm spacing, feeding and hot tearing properties of aluminum alloys. *Quality Control of Engineering Alloys and the Role of Metals Science*, 131-145.
- Ficher, F. D., Reisner, G., Werner, E., Tanaka, K., Cailletaud, G., & Antretter, T. (2000, June 1). A new view on transformation induced plasticity (TRIP). *International Journal of Plasticity*, 16(7-8), 723-748. doi:10.1016/S0749-6419(99)00078-9
- Fisher C. John. (1948). The Fracture of Liquids. Journal of applied Physics, 19, 1062-1067. doi:10.1063/1.1698012
- Fotovvati, B., Wayne, S. F., Lewis, G., & Asadi, E. (2018, April 2). A Review on Melt-Pool Characteristics in Laser Welding of Metals. (P. Ferro, Ed.) *Advances in Materials Science and Engineering*, 4920718. doi:10.1155/2018/4920718
- Fuhrich, T., Berger, P., & Hügel, H. (2001, October 01). Marangoni effect in laser deep penetration welding of steel. *Journal of Laser Applications*, 13, 178-186. doi:10.2351/1.1404412
- Girault, E., Mertens, A., Jacques, P., Houbaert, Y., Verlinden, B., & van Humbeect, J. (2001, April 1). Comparison of the effects of silicon and aluminium on the tensile behaviour of multiphase TRIP-assisted steels. *Scripta Materialia*, 44(6), 885-892. doi:10.1016/S1359-6462(00)00697-7
- Hahn, D. W., & Özisik, M. (2012). *Heat conduction*. Hoboken, New Jersey, the United States of America: John Wiley & Sons.
- Ismail, M., Okamoto, Y., Okada, A., & Uno, Y. (2011). Experimental Investigation on Micro-Welding of Thin Stainless-Steel Sheet by Fiber Laser. *American Journal of Engineering and Applied Sciences*, 4, 314-320.
- Jacques, P. J. (2004, June-August). Transformation-induced plasticity for high strength formable steels. *Current Opinion in Solid State and Materials Science*, 8(3-4), 259-265. doi:10.1016/j.cossms.2004.09.006
- Jacques, P. J., Girault, E., Mertens, A., Verlinden, B., van Humbeeck, J., & Delannay, F. (2001). The Developments of Cold-rolled TRIP-assisted Multiphase Steels. Alalloyed TRIP-assisted Multiphase Steels. *ISIJ International*, 41(9), 1068-1074. doi:10.2355/isijinternational.41.1068
- Johnson, P. B., & Christy, R. W. (1974, July 15). Optical constants of transition metals: Ti, V, Cr, Mn, Fe, Co, Ni, and Pd. *Physical Review B*, 9(12), 5056. doi:10.1103/PhysRevB.9.5056
- Kannengießer, T., & Böllinghaus, T. (2014). Hot cracking tests—an overview of present technologies and applications. *Welding in the World, 58*, 397-421.
- Keivanloo, A., Naffakh-Moosavy, H., & Miresmaeili, R. (2021, November). The effect of pulsed laser welding on hot cracking susceptible region size and weld pool internal geometry of Inconel 718: Numerical and experimental approaches. *CIRP Journal of Manufacturing Science and Technology*, 35, 787-794.

- Khan, M. S., Ali, S., Westerbaan, D., Duley, W., Biro, E., & Zhou, Y. N. (2022, June). The effect of laser impingement angle on the optimization of melt pool geometry to improve process stability during high-speed laser welding of thin-gauge automotive steels. *Journal of Manufacturing Processes*, 78, 242-253. doi:10.1016/j.jmapro.2022.04.022
- Kim, H., & Nam, S. (1996). Solidification cracking susceptibility of high strength aluminum alloy weldment. *Scripta Materialia*, 34(7), 1139-1145.
- Kirchhoff, M. (2013). Laser applications in battery production—From cutting foils to welding the case. 2013 3rd international electric drives production conference, 1-3.
- Konopka, J. (2013). Options for Quantitative Analysis of Light Elements by SEM/EDS. *Technical Note*, 52523.
- Kou, S. (2003). *Welding metallurgy* (Vol. 431). New Jersey, USA: Cambridge University Press.
- Kou, S. (2015). A criterion for cracking during solidification. *Acta Materials*, 88, 366-374.
- Kripalani, K., & Jain, P. (2021). Comprehensive study of laser cladding by nitinol wire. *Materials Today: Proceedings*, *37*(2), 656-664. doi:10.1016/j.matpr.2020.05.631
- Kumar, N., Mukherjee, M., & Bandyopadhyay, A. (2017, September 1). Study on laser welding of austenitic stainless steel by varying incident angle of pulsed laser beam. *Optics & Laser Technology*, *94*, 296-309. doi:10.1016/j.optlastec.2017.04.008
- Lancaster, J. (1984). The Physics of Welding. Physics in Technology, 15, 73-79.
- Lee, J., Sohn, S., Hong, S., Suh, B.-C., Kim, S.-K., Lee, B.-J., . . . Lee, S. (2014, August 19). Effects of Mn Addition on Tensile and Charpy Impact Properties in Austenitic Fe-Mn-C-Al-Based Steels for Cryogenic Applications. *Metallurgical and Materials Transactions A*, 45, 5419-5430. doi:10.1007/s11661-014-2513-9
- Lei, J., Liu, G., Li, H., Han, H., Di, R., & Lei, J. (2023). Gaussian and circular oscillating laser directed energy deposition of WC/NiCu composites. *Materials Characterization*, 204, 113218. doi:10.1016/j.matchar.2023.113218
- LePera, F. S. (1979, September). Improved etching technique for the determination of percent martensite in high-strength dual-phase steels. *Metallography*, 12(3), 263-268. doi:10.1016/0026-0800(79)90041-7
- Li, S., Mi, G., & Wang, C. (2020, May). A study on laser beam oscillating welding characteristics for the 5083 aluminum alloy: Morphology, microstructure and mechanical properties. *Journal of Manufacturing Processes*, 53, 12-20. doi:https://doi.org/10.1016/j.jmapro.2020.01.018
- Liang, X. (2024). Solidification modelling in metallic melt-pools: with application to welding and additive manufacturing. Delft: TU Delft.
- Liao, Y.-C., & Yu, M.-H. (2007, July 23). Effects of laser beam energy and incident angle on the pulse laser welding of stainless steel thin sheet. *Journal of Materials Processing Technology*, 190(1-3), 102-108. doi:10.1016/j.jmatprotec.2007.03.102
- LippoldJohn C. (2015). Welding Metallurgy and Weldability. Columbus, Ohio, United States: Ohio State University.
- Liu, L., He, B., & Huang, M. (2018, March 26). The Role of Transformation-Induced Plasticity in the Development of Advanced High Strength Steels. *Advanced Engineering Materials*, 20(6), 1701083. doi:10.1002/adem.201701083

- Luo, Y., Zhu, L., Han, J., Xu, J., Zhang, C., & Chen, D. (2019). Effect of focusing condition on laser energy absorption characteristics in pulsed laser welding. *Optics & Laser Technology*, 117, 52-63.
- Mahrle, A., & Beyer, E. (2009). Theoretical aspects of fibre laser cutting. *Journal of Physics D: Applied Physics*, 42, 175507. doi:10.1088/0022-3727/42/17/175507
- ManitsasDimosthenis, & AndersonJoel. (2018). Hot Cracking Mechanisms in Welding Metallurgy: A Review of Theoretical Approaches. MATEC web of conferences, 188, 03018.
- Miyamoto, I. (2013). 11 Laser welding of glass. In S. Katayama, *Handbook of Laser Welding Technologies* (pp. 301-331). Osaka, Japan: Woodhead Publishing Series in Electronic and Optical Materials. doi:10.1533/9780857098771.2.301
- Muhammad, Z.-u.-a., Daniel, N., Jean-François, J., & Dominique, D. (2010, May 15). Experimental investigation and finite element simulation of laser beam welding induced residual stresses and distortions in thin sheets of AA 6056-T4. *Materials Science and Engineering:* A, 527(12), 3025-3039. doi:10.1016/j.msea.2010.01.054
- Pakniat, M., Ghanini, F. M., & Torkamany, M. J. (2016, September 15). Hot cracking in laser welding of Hastelloy X with pulsed Nd:YAG and continuous wave fiber lasers. *Materials & Design*, 106, 177-183. doi:10.1016/j.matdes.2016.05.124
- PanYu. (2011). Laser Welding of Zinc Coated Steel wthout a Pre-set Gap. PhD Thesis TUD.
- Pellini, W. S. (1952). Strain Theory of Hot Tearing. Foundry, 80(11), 125-133.
- Prokhorov, N. N. (1956). The problem of the strength of metals while solidifying during welding. *Svarochnoe Proizvodstvo*, 6, 5-11.
- Pumphrey, W. (1948). A consideration of the nature of brittleness at temperatures above the solidus in castings and welds in aluminium alloys. *J. of the Inst. of Metals*, 75, 235-256.
- Rappaz, M., & Dantzig, J. (2009). Solidification. Lausanne: EPFL Press.
- Rappaz, M., Drezet, J., & Gremaud, M. (1999, Feburary). A new hot-tearing criterion. *Metallurgical and Materials Transactions A*, 30, 449-455.
- Ren, Z., Zhang, D. Z., Fu, G., Jiang, J., & Zhao, M. (2021, September). High-fidelity modelling of selective laser melting copper alloy: Laser reflection behavior and thermal-fluid dynamics. *Materials & Design*, 207, 109857. doi:10.1016/j.matdes.2021.109857
- Schaefer, M., Kessler, S., Scheible, P., & Graf, T. (2017, October 27). Modulation of the laser power to prevent hot cracking during laser welding of tempered steel. *Journal of Laser Applications*, 29(4), 042008.
- Schaefer, M., Kessler, S., Scheible, P., Speker, N., & Harrer, T. (2017, Feburary). Hot cracking during laser welding of steel: Influence of the welding parameters and prevention of cracks. *High-Power Laser Materials Processing: Applications, Diagnostics, and Systems VI, 10097*, 111-118.
- Schempp, P., Cross, C., Pittner, A., Oder, G., Neumann, R., Rooch, H., . . . Rethmeier, M. (2014). Solidification of GTA aluminum weld metal: Part 1—Grain morphology dependent upon alloy composition and grain refiner content. *Welding Journal*, 93(2), 53s-59s.

- Schobbert, H., Böllinghaus, T., & Wolf, M. (2003). Hot cracking resistance of laser and hybrid welded austenitic stainless steels. *Trends in welding research-Proceedings of the 6th international conference*, 76-81.
- Senda, T., Matsuda, F., & Takano, G. (1973). Solidification Crack Susceptibility for Weld Metals With the Trans-Varestraint Test. *Yosetsu Gakkai- Shi*, 42(1), 48-56.
- ShihYungjen. (2013). Mitigation of hot cracking of alloy 52M overlay on cast stainless steel CF8A. Science and Technology of Welding and Joining, 18(7), 566-572.
- Soleimani, M., Kalhor, A., & Mirzadeh, H. (2020, September 23). Transformation-induced plasticity (TRIP) in advanced steels: A review. *Material Science and Enginering:* A, 795, 140023. doi:10.1016/j.msea.2020.140023
- Spina, R., Tricarico, L., Basile, G., & Sibillano, T. (2007). Thermo-mechanical modeling of laser welding of AA5083 sheets. *Journal of materials processing technology*, 191(1-3), 215-219.
- Stelling, K., Böllinghaus, T., Wolf, M., Schöler, A., Burkert, A., Burkert, A., & Isecke, B. (2005). Hot cracks as stress corrosion cracking initiation sites in laser welded corrosion resistant alloys. *Hot Cracking Phenomena in Welds*, 165-182.
- Sugimoto, K.-i., Usui, N., Kobayashi, M., & Hashimoto, S.-i. (1992). Effects of Volume Fraction and Stability of Retained Austenite on Ductility of TRIP-aided Dualphase Steels. *ISIJ International*, 32(12), 1311-1318. doi:10.2355/isijinternational.32.1311
- Takahashi, M., & Bhadeshia, H. (1991). A Model for the Microstructure of Some Advanced Bainitic Steels. *Materials Transactions*, *JIM*, *32*(8), 689-696. doi:10.2320/matertrans1989.32.689
- Timokhina, I. B., Hodgson, P. D., & Pereloma, E. V. (2004, August). Effect of microstructure on the stability of retained austenite in transformation-induced-plasticity steels. *Metallurgical and Materials Transactions A*, *35*, 2331-2341. doi:10.1007/s11661-006-0213-9
- Trapp, J., Rubenchik, A. M., Guss, G., & Matthews, M. J. (2017). In situ absorptivity measurements of metallic powders during laser powder-bed fusion additive manufacturing. *Applied Materials Today*, *9*, 341-349. doi:10.1016/j.apmt.2017.08.006
- Vâlsan, D., Bolocan, V., Burcă, M., & Crăciunescu, C. (2023). Experiments on Nd:YAG pulsed laser welding of thin sheets. *Materials Today: Proceedings*, 78(2), 295-301.
- WallAndrew, & BenoitJ.Michael. (2023). A review of existing solidification crack tests and analysis of their transferability to additive manufacturing. Journal of Materials Processing Technology, 320, 118090.
- Wang, D., Zhang, F., Warinsiriruk, E., Zhu, Q., Li, T., Li, H., ... Yang, S. (2024). A novel method for evaluating solidification cracking susceptibility of austenitic stainless steel using trapezoidal hot cracking test during laser welding. *Optics & Laser Technology*, 175, 110789. doi:10.1016/j.optlastec.2024.110789
- Wang, J., Zhang, M., Wang, H., Li, Z., Cheng, X., Zhang, B., . . . Ran, X. (2022). Mitigating hot-cracking of laser melted CoCrFeNiMnTix high-entropy alloys. *Materials Letters*, 314, 131771.
- Xie, J., Kar, A., Rothenflue, J., & Latham, W. (1997). Temperature-dependent absorptivity and cutting capability of CO2, Nd:YAG and chemical oxygen-iodine lasers. *Journal of Laser Applications*, 9(2), 77-85. doi:10.2351/1.4745447

- Xinhua News. (2024, January 20). *Zhuque-3 reusable rocket completes vertical return technology test*. Retrieved from Xinhuanet: https://english.news.cn/20240120/1a7836ed4fe34c30b769d73e53e211f5/c.html
- Xue, B., Chang, B., Wang, S., Hou, R., Wen, P., & Du, D. (2022, March 25). Humping Formation and Suppression in High-Speed Laser Welding. *Materials*, 15(7), 2420. doi:10.3390/ma15072420
- Yang, Z., Bauereiß, A., Markl, M., & Körner, C. (2021, March 12). Modeling Laser Beam Absorption of Metal Alloys at High Temperatures for Selective Laser Melting. *Advanced Engineering Materals*, 23(9), 2100137. doi:10.1002/adem.202100137
- Yao, Z., Wang, Z., Chen, J., Sui, Y., & Yao, J. (2022, January). Equiaxed microstructure formation by ultrasonic assisted laser metal deposition. *Manufacturing Letters*, *31*, 56-59. doi:10.1016/j.mfglet.2021.07.002
- Zacharia, T. (1994). Dynamic Stresses in Weld Metal Hot Cracking. Welding Journal Including Welding Research Supplement, 73(7), 164-172.
- Zhang, P., Jia, Z., Yu, Z., Shi, H., Li, S., Wu, D., . . . Tian, Y. (2021, August). A review on the effect of laser pulse shaping on the microstructure and hot cracking behavior in the welding of alloys. *Optics & Laser Technology*, 140, 107094.
- Zhao, D., Wu, L., Zhang, T., Kong, L., & Liu, Y. (2022, February 10). Effect of Preheating on Hot Cracking Susceptibility in Pulsed Laser Welding of Invar Alloy. *Journal of Ship Production and Design*, 38(01), 19-27. doi:10.5957/JSPD.01200002
- Zhu, Z., Liu, Y., Gou, G., Gao, W., & Chen, J. (2021, May 11). Effect of heat input on interfacial characterization of the butter joint of hot-rolling CP-Ti/Q235 bimetallic sheets by Laser + CMT. *Scientific Reports*, 11(1), 10020.

